MASSACHUSETTS INSTITUTE OF TECHNOLOGY
AEROPHYSICS LABORATORY

Technical Report 130

AN INVESTIGATION OF FORCES ON AN OSCILLATING CYLINDER FOR APPLICATION TO GROUND WIND LOADS ON LAUNCH VEHICLES

by

Leon H. Schindel
Garabed Zartarian
Peter K. S. Wu

Contract No. NAS8-20186
MIT DSR 74956

October 1966

Massachusetts Institute of Technology
Department of Aeronautics and Astronautics
Aerospace Research Division
Aerophysics Laboratory

Technical Report 130

AN INVESTIGATION OF FORCES ON AN OSCILLATING CYLINDER FOR APPLICATION TO GROUND WIND LOADS ON LAUNCH VEHICLES

by

Leon H. Schindel
Garabed Zartarian
Peter K. S. Wu

Contract No. NAS8-20186
MIT DSR 74956

October 1966

FOREWORD

The research reported here was sponsored by the George C. Marshall Space Flight Center of the NASA under Contract NAS8-20186. The project was monitored for the NASA by Dr. Max F. Platzer and Mr. James C. Young. Prof. Morton Finston of M.I.T. was faculty supervisor, and the principal investigator for M.I.T. was Dr. Leon H. Schindel. Part of the work was performed, under subcontract, at Boston University. Mr. Garabed Zartarian was principal investigator for Boston University.

ABSTRACT

The effects of model motion on the forces acting on a two-dimensional cylinder are investigated for application to the prediction of ground wind loads on launch vehicles. The wakes behind stationary and oscillating circular cylinders are studied with the aid of a hydrogen bubble flow visualization technique. The paths of wake vortices are examined for a cylinder with a small amplitude negatively-damped oscillation, a larger amplitude damped oscillation, and an oscillation of intermediate amplitude with approximately zero damping. A multiple-vortex analytical model is devised with which it is possible to calculate the periodic motion of the wake vortices and the resulting forces on a stationary cylinder. Possible extensions of the method to the case of an oscillating cylinder are indicated.

TABLE OF CONTENTS

LIST OF ILLUSTRATIONS

LIST OF PRINCIPAL SYMBOLS

A	amplitude of cylinder oscillation
A_{cr}	amplitude of free oscillation
A_o	amplitude of free oscillation in the absence of structural damping
a	cylinder radius; downstream distance from center of cylinder to vortex
C_a	hydrodynamic damping coefficient
C_D	drag coefficient on stationary cylinder
C_ℓ	amplitude of lift coefficient
D	cylinder diameter; drag on cylinder
D'	nondimensional diameter of cylinder representing neighboring structure
F_a	lateral hydrodynamic force
f_a	amplitude of lateral hydrodynamic force
f_N	natural frequency of cylinder and support system
f_s	Strouhal frequency
i	imaginary unit, $\sqrt{-1}$
I	total impulse
$\mathcal{I}m$	imaginary part of
L	lift (lateral force) on cylinder
ℓ	nondimensional distance between cylinders (see Sketch G)
m_a	virtual mass (= mass of fluid displaced by cylinder)
Q_j	nondimensional velocity at vortex j, $Q_j = Q_{jr} + i\,Q_{ji}$
Re	Reynolds number; real part of
r	nondimensional rate of vorticity generation

St	Strouhal number
t	time
t_b	time at which vortex breaks away from its feeding sheet
t_p	period of flow oscillation
t_1	time at which oscillating cylinder crosses its mid position
u	y-component of flow velocity
V_0	free stream velocity
v	z-component of flow velocity
w	complex velocity potential
Y	amplitude of lateral oscillation
y, z	components of complex coordinate, $\zeta = y + iz$
α	direction of stream relative to moving cylinder
Γ	vortex strength
Γ_c	strength of farthest vortex
Γ_{c_i}	strength of image of Γ_c
γ	dummy mass fraction
η_f	nondimensional feeding point
η_0	nondimensional separation point
η_s	nondimensional position of vortex s, $\eta_s = \eta_{sr} + i\,\eta_{si}$
ζ	position in complex plane
ζ_c	position of farthest vortex
ζ_{c_i}	position of image of vortex at ζ_c
ζ_{01}	separation point for vortex 1
ζ_{02}	separation point for vortex 2

LIST OF PRINCIPAL SYMBOLS (Concluded)

θ angular location of neighboring structure (see Sketch G)

θ_o angular coordinate of separation point for Γ

λ nondimensional vortex strength (see Eq. 9a)

ρ stream density

τ nondimensional time = $\frac{Vt}{a}$

Φ velocity potential

ϕ phase angle between force and displacement (see Eqs. 2 and 3)

ϕ' phase angle with dummy mass added to system

Ψ stream function

ψ mass ratio (see Section II)

ω angular frequency of cylinder oscillation

SECTION I

INTRODUCTION

In their report on a ground wind loads program at the Langley Research Center, Foughner and Duncan (Ref. 1) show a photograph of a surplus Thor vehicle which has been toppled by a wind storm. Since this Thor was being used at the time in a study of ground wind loads on erected launch vehicles, its destruction may have served a useful purpose. The possibility of a similar catastrophe causing the sudden demise of an expensive space mission, however, is somewhat disquieting.

While an erected launch vehicle (such as that depicted in Fig. 1) might conceivably be blown over by a sufficiently violent gust of wind, an oscillating side load presents a more dangerous threat. An oscillatory load accompanies the alternate shedding of vortices from the sides of a cylindrical body. The wake forms the so-called Karman vortex street. Such oscillatory loads have been responsible for failures of tall chimneys and are also the causes in the somewhat related problems of galloping transmission lines and collapsing bridges (most notably the Tacoma Narrows Bridge); but these latter situations arise primarily from aerodynamic nonsymmetry and body motion.

When a vortex "peels off" from one side of a stationary circular cylinder*, the lateral symmetry of the flow pattern is destroyed so that a net pressure force appears on the body. This force generally has a small component in the downstream (drag) direction and a much larger lateral (lift) component. A short time later a vortex is released from the opposite side of the cylinder, reversing the direction of the side force. This alternating lateral load is sometimes referred to as the "Strouhal force", named after the man who first investigated the phenomenon in 1878 (cf. Ref. 2).

---

* Or a cylinder symmetric about a line parallel to the stream.

The antisymmetric wake behind a stationary circular cylinder in two-dimensional flow and the accompanying lateral forces have a dimensionless frequency which is nearly constant when the flow is laminar. This particular reduced frequency, called the Strouhal number and designated as St, is close to 0.2 over a Reynolds number range of approximately $100 < Re < 100,000$ for smooth cylinders. In this subcritical Reynolds number range then, the vortex shedding frequency f_s, is approximately $f_s \sim \frac{0.2V_0}{D}$, where D is the cylinder diameter, and V_0 the flow velocity. Thus, for a given diameter, the frequency is directly proportional to the velocity V_0.

Launch vehicles are susceptible to "large excitations" at low wind speeds because of their low natural frequencies and low structural dampings. This point becomes apparent when one considers the vehicle as a second order linear system in a simplified analysis. It is a well-known result that for small damping ratios, the sinusoidal responses are maximum when the forcing frequency is near the natural frequency of the system. Since low frequencies imply low speeds, it is not difficult to foresee (from very approximate calculations using ranges of typical parameters) possible large lateral motions of these vehicles at relatively low wind velocities. Furthermore, since the damping coefficients are small, even oscillatory aerodynamic forces of moderate amplitudes can result in sufficiently large stress peaks to cause destruction of the launch vehicle.

A complete description of the Strouhal force on a stationary cylinder in two-dimensional flow is not sufficient to prescribe the lateral aerodynamic force on an actual launch vehicle. For example, three-dimensional effects, particularly around the nose of the missile, can be significant, as pointed out by some investigators (cf. Buell, Ref. 3 and Blackiston, Ref. 4). Among other complicating three-dimensionality features are the effects of ground wind velocity gradients and variations in vehicle cross-sectional dimensions. The ground wind also varies randomly in space and time, having in its spectrum gusts with frequencies in a range including the natural frequency of the structure. Some effects of random gusts were studied some years ago by Fung (Ref. 5) and his colleagues. Another important consideration is the effect of cylinder's

own motion on the aerodynamic forces, and this area has been studied by Meier-Windhorst (Ref. 6) and Bishop and Hassan (Refs. 7, 8). The present investigation is also an attempt to contribute to the understanding of the latter problem.

The aerodynamic analysis may become even more formidable when the situations encountered occur at higher Reynolds numbers. The periodicity present at subcritical Reynolds numbers breaks down, and random vortex shedding appears in the so-called critical range ($10^5 < Re < 3.5 \times 10^6$). At still higher Re's, Roshko's tests (Ref.9) revealed reappearance of the periodic shedding, although partially obscured by turbulence. In the latter range, Roshko found the Strouhal number to be approximately 0.3. During transition from laminar to fully turbulent flow (i.e., in the critical range), the Strouhal forces are "elusive" and the dominant reduced frequency in the spectrum of the random forces varies, apparently decreasing in some cases to a low value of 0.1. Photographs of wake patterns at various Reynolds numbers and a discussion of their characteristics may be found in Ref. 10.

Because of the potentially destructive effects of these oscillatory loads, much effort has been expended in analytical and experimental aeroelastic simulation techniques. Scruton (Ref. 11) and Whitbread (Ref. 12) summarize much of the available data in their aeroelastic studies of wind-driven structures (such as towers, chimneys, masts). In their analyses, they utilize experimentally-determined forms for the effect of structural motion on the Strouhal forces. Reid (Ref. 13) follows a somewhat similar approach in an analog-computer solution of the problem. The last reference is also one of many reporting on wind tunnel experiments simulating the effects of ground wind loads and experiments on full-scale vehicles in natural winds (cf. Refs. 3, 14, 15 which were papers presented at a Meeting on Ground Wind Load Problems in Relation to Launch Vehicles, held at NASA Langley Research Center on June 6-7, 1966*).

* The proceedings of this meeting contain in addition other papers pertinent to this subject.

These findings emphasize the importance of the aerodynamic excitations and the desirability of understanding their origin and development. Strouhal forces on stationary cylinders have been measured by Keefe (Ref. 16), Macovsky (Ref. 17), Humphries (Ref. 18), Gerrard (Ref. 19), who also measured pressures. These measurements at subcritical Re's show sinusoidal variations in the lateral force at the Strouhal frequencies, with dimensionless (single) amplitudes of approximately 0.6 based on cross-sectional area and free-stream dynamic pressure. The Strouhal oscillations in some instances were superimposed on signals of other frequencies. The results differ, from one experimenter to another, even within this relatively simpler range of Reynolds number. The oscillatory loads were found to be very sensitive to end conditions, such as gap effects, and other seemingly insignificant devices or conditions needed to support the cylinder and measure the forces.

Since the present investigation is concerned with the effects of motion, measurements of the lateral forces on oscillating cylinders are more directly applicable. An important early experiment is described by Meier-Windhorst (Ref. 6). He measured the amplitude and frequency of elastically-supported cylinders in a water channel flow. Slowly raising the flow velocities, he found large increases in response amplitudes when the Strouhal number coincided with the reduced natural frequency of the model and its support. The large amplitudes persisted beyond this point, however, even rising slightly over the next 10 percent increase in velocity. Furthermore, the frequency of the model's oscillation was not observed to vary in direct proportion with the velocity, a variation expected from the Strouhal frequency f_s. Thus, the oscillatory motion, once established, tended to stabilize the frequency of the vortex shedding to some value near the natural frequency of the system*. The instantaneous pressure measurements of Bishop and Hassan (Ref. 7) on sinusoidally-driven circular cylinders verify this "frequency-locking" phenomenon.

* For higher mass ratios, γ, (see Section II), the vortex shedding frequency is expected to stay closer to the natural frequency of the system.

Other investigations, dealing with force measurements on oscillatory cylinders that should be mentioned, are those of Parkinson and Ferguson (Ref. 20) at subcritical Re's and Cincotta et al (Ref. 21) at higher Re's.

An understanding of the nature of the flow about an oscillating cylinder is essential to arrive at answers to the following important questions:

1. How are the periodic, two-dimensional Strouhal forces on a stationary circular cylinder modified by an oscillating motion of the cylinder near the Strouhal frequency.
2. Under what circumstances, if any, might an oscillatory motion of the cylinder removed from the Strouhal frequency alter the flow field so as to introduce periodic aerodynamic forces which tend to abet the motion. If such forces are "stabilizing", to what extent do they damp the motion if all other excitation forces are removed.

The present investigation substantiates in some areas the extensive exploratory work of Bishop and Hassan (Ref. 7). It also compliments the latter in the area of wake visualization. Clues to the character of the vortex wake are provided by streaklines made visible by paths of hydrogen bubbles. Analytical descriptions of the flow have been formulated on the basis of these observations. These formulations are then used to predict vortex paths and forces on the stationary cylinder and to compare them with experimental data.

In this initial attempt, the case of the stationary cylinder was analyzed in detail since considerable computer programming and numerical work were found to be required even without the complication of cylinder motion. Actually, two mathematical models were pursued, one based on an extension of Bryson's theory (Ref. 22) for the symmetric vortex shedding, and the other representing a simplification of Ujihara's model (Ref. 23). Possible procedures for extending the methods to the case of the oscillating cylinder are indicated.

The experimental arrangements and results are described in the next section. Details of the flow behind stationary and oscillating cylinders

are given. These visual data are supplemented with force and displacement measurements on both free and driven cylindrical models. The influence of a neighboring structure, such as an umbilical tower, was also studied and some limited data are presented.

Two analytical models are described in detail in Section III. Machine calculations based on one of the formulations are compared with the experimental forces and vortex positions for the stationary cylinder. Possible extensions to the oscillatory case are indicated.

The final section presents a summary of the results and the corresponding conclusions.

SECTION II

EXPERIMENTAL TECHNIQUES AND RESULTS

In his experiments, Meier-Windhorst (Ref. 6) observed the free oscillations of an elastically-mounted cylinder in an 18-cm deep water channel flow, for various combinations of cylinder mass, cylinder natural frequency and of built-in viscous damping. For each case he tried to establish the dependence of amplitude and frequency of oscillations on the free-stream velocity. Some features of his results of interest to the present study are:

(1) When the velocity was increased slowly, a critical velocity was reached where the amplitude rose sharply. This point corresponded to a motion frequency equal to the natural frequency of the system in still water, f_N , and also equal to the Strouhal frequency f_S [$= \frac{(St)V_o}{D}$, where V_o is the free-stream velocity, D the diameter and (St) the Strouhal number] .

(2) As the velocity was increased somewhat further, the amplitudes of motion increased slowly. The motion frequency was found to be somewhere between the Strouhal frequency and the natural frequency, being closer to the latter for higher mass ratios. For still higher velocities, amplitudes dropped gradually.

(3) The mass ratio, ψ , defined as

$$\psi = \frac{\text{Mass of the cylinder + reduced mass of oscillating arm}}{\text{Mass of displaced fluid}} + 1,$$

varied from about 2.3 to 8.8*. With increasing ψ , the width of the amplitude vs. V_o curve, the maximum amplitude, and the difference between motion frequency and natural frequency decreased.

---

* In the experiments to be described later, ψ was estimated to be around 300-400.

It is apparent from these results that the cylinder response to the hydrodynamic forces is not strictly speaking due to a resonance effect. Stated alternatively, the cylinder motion alters the flow field significantly, and the vortex shedding frequency is generally different from both f_N and f_S. One would also expect changes in the equivalent hydrodynamic damping force. For present purposes, it is adequate to express the total hydrodynamic force F_a as a function of the displacement y by

$$F_a = -m_a \ddot{y} - c_a \dot{y} \qquad (1)$$

where c_a is the hydrodynamic damping coefficient, and m_a is the virtual mass defined as the mass of fluid displaced by the cylinder. The two terms represent the parts in phase with acceleration $\ddot{y}$ and with velocity $\dot{y}$ respectively. Scruton (Ref. 11) has adopted this type of division in his analysis and presentation of experimental results on aerodynamic derivatives. It's use can be justified only when the amplitudes are large and the dominant forces are of the same frequency as the motion. At lower amplitudes, unless motion and Strouhal frequencies are very close, the force signal will contain both frequencies, and Eq. (1) is no longer useful. At reduced frequencies sufficiently close to the Strouhal number, c_a will have a negative sign at low amplitudes. With increasing amplitude, c_a will increase and reverse in sign at some amplitude which will be denoted here by A_o. In the absence of structural damping forces in the system, A_o would be the maximum attainable amplitude in free oscillation.

One important objective in the present investigation was to determine approximately the hydrodynamic zero-damping boundary as a function of reduced frequency, or equivalently the lines where $c_a = 0$ in an amplitude versus reduced frequency plot. Having established the regions of negative c_a, the next task was to examine by flow visualization the wake pattern (the shedding process) in such cases. The results of the flow-visualization study were then used in an attempt to formulate a simple analytical model capable of predicting the aforementioned $c_a = 0$ -boundaries, as well as the magnitudes of the oscillatory forces.

II.1 APPARATUS

II.1.1 Water Table

The water table used in the present experiments* (Fig. 2) had a flow channel 36 inches long and 12 inches wide in which water depths of up to 0.9 inches could be obtained. The floor of the channel was made of 1/4 inch plate glass so that the hydrogen bubbles could be properly illuminated during flow visualization runs. The velocity of the tests ranged from about 5.0 in/sec to 11.5 in/sec, with corresponding Reynolds numbers (based on the cylinder diameter) of approximately 4.8×10^3 to 11×10^3. At the lower portion of the velocity range, a small dam, 1/4 inch in height, was used to raise the water level. It did not cause any observable disturbance in the velocity profile in the test section.

The free stream velocity was calibrated by Roshko's method (Ref. 25) which needs only the vortex shedding frequency, f_s, behind a stationary circular cylinder. Experimental data have shown that the Strouhal number, St, is nearly independent of Reynolds number in the range $300 < Re < 10^5$. According to Roshko, this Strouhal number is equal to 0.212, with maximum deviations amounting to about 4 percent for $Re \simeq 10^4$. The procedure was checked approximately by timing a pulse of hydrogen bubbles travelling a premarked distance.

In the course of this experiment, surface waves were observed especially when the model was oscillating at high amplitudes and/or at high frequencies. They were eliminated by placing a piece of plexiglas on top of the water. However, the plexiglas imposed another undesirable boundary layer on the flow. An estimate, based on a flat plate analogy, indicated that about 70 percent of the water depth was inside the boundary layers along the plexiglas and channel floor, and at the test section. This did not provide a good two-dimensional flow. Gaps had also a large influence on the flow. The surface effect (and possibly the gap effect) could have been reduced by increasing the water depth in the channel.

---

* Some of the results given here are treated in more detail in Ref. 24.

II.1.2 Pendulum

A model support and drive system was required to drive the model sinusoidally. It was also necessary to provide a means for measuring the hydrodynamic forces associated with the oscillatory motion of the model. After some investigations and trials, a flexure-supported pendulum was adopted. It had the following advantages:

(1) It provided a smooth low noise sinusoidal motion at or near its natural frequency.

(2) It could be driven easily by an eccentric weight.

(3) It had negligible friction, allowing free oscillations of appreciable amplitude to develop even with the small hydrodynamic forces present ($\sim 2 \times 10^{-3}$ lb).

(4) It was comparatively easy to construct.

(5) It provided a wide range of frequency (approximately 0.7 cps to 5.0 cps).

The pendulum (Fig. 3) was made of a 15 lb steel rod, 5 feet 2 inches in length and one inch in diameter. The upper end of the rod was connected to an 8 inch long flexure.

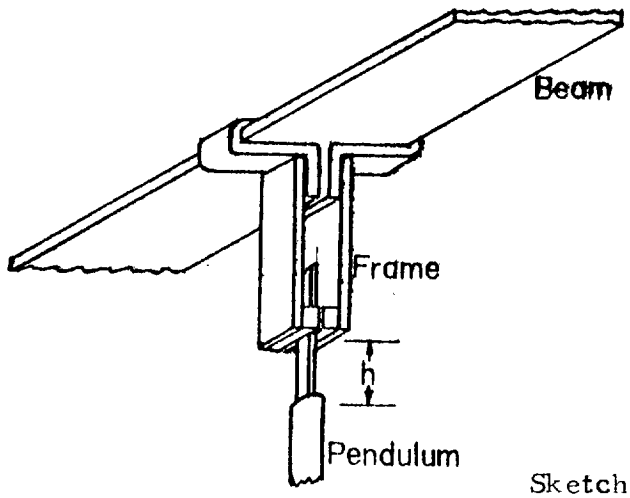

Sketch A

The flexure was supported by a rigid frame (see Sketch A). The upper end of the frame was fastened to a beam in the building and its lower end held firmly the flexure. The effective length, h, (the portion of the flexure below the frame), which could be varied by raising or

lowering the flexure, controlled the natural frequency of the pendulum.

The pendulum was caused to oscillate by an eccentric weight which rotated in a plane perpendicular to the free stream of the water table. The platform which supported the driving gears was located approximately at the center of percussion of the pendulum so as to limit the oscillations to the fundamental mode of the pendulum. The eccentric weight was, in turn, driven by a DC motor through a series of belts. By varying the power input to the motor, one could control the rpm of the motor and hence the speed of the eccentric weight. As a result, both the frequency and the amplitude of the motion could be adjusted to obtain desirable ranges.

The model was clamped to the lower end of the pendulum. Forces on the model were measured by a strain gage balance system which will be described in the next section, while it's displacements were obtained from the deflection of a light ray reflected from mirrors mounted on the support.

II.1.3 Model Description

The model (Fig. 4) consisted of two identical hollow 1/16 inch thick brass cylinders connected by a 3/64 inch thick and 7/32 inch wide rectangular aluminum bar. The cylinders were 1.5 inch in diameter and 1.1 inch in height. The reason for mounting the two cylinders symmetrically with respect to the support was to subtract the inertia force of the top cylinder from that of the bottom one such that the net recorded force on the bottom cylinder was due solely to the hydrodynamic forces. Strain gages were used to measure these forces and were mounted symmetrically above and below the point at which the aluminum bar was supported.

The aluminum bar was required to remain rigid, but at the same time to have sufficient deflection so that the response in the strain gages could be traceable on an oscilloscope. Its natural frequency ($\simeq$ 50 cycle sec) was much higher than the frequency of the entire system (less than 5 cycle/sec). The lower cylinder was sealed at the ends to avoid water splash against its inside wall during oscillations.

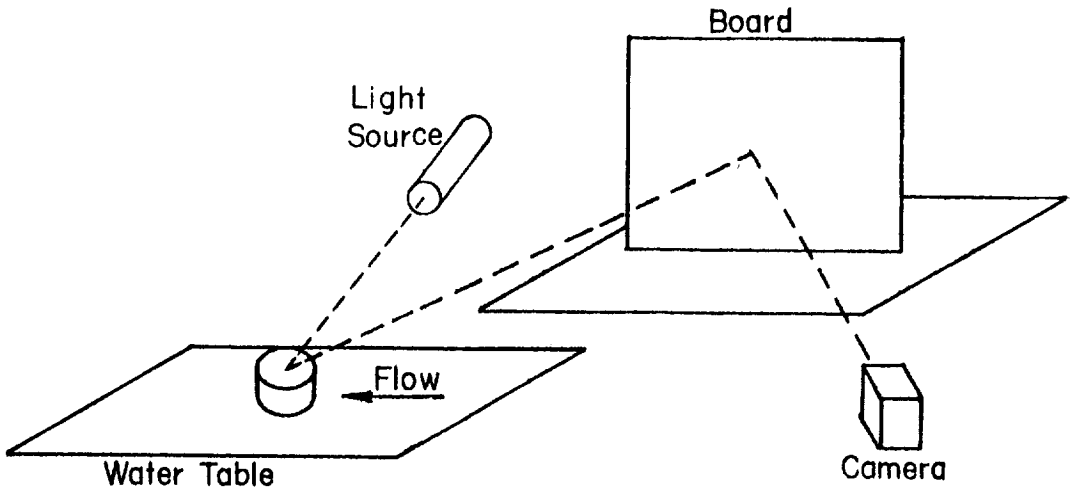

Sketch B

II.1.4 Instrumentation

Two 3/16 inch diameter concave mirrors were mounted on the model-supporting frame of the pendulum. The upper one provided a means of indicating the phase relationship between the force and the displacement of the cylinder. The lower one provided the amplitude measurements. These mirrors reflected light from a source onto a board with point images because the board was located at the focal distance (see Sketch B). As the pendulum oscillated the (moving) lower point on the board was photographed by a rotating camera. Thus, the instantaneous deflection was recorded. A damped oscillation trace obtained in this manner is shown in Fig. 5a.

A photocell was placed below the neutral position of the upper point. A small current was induced whenever the point crossed the photocell. The signal was fed into a dual-beam oscilloscope together with the input from the strain gages on the model. Figure 5b shows a typical oscilloscope trace. The sinusoidal curve represents the force as a function of time (the noise is electrical and was present with no signal). The "blips" on the displacement trace occur at times when the light ray crosses the photocell. One extreme of the displacement is noted halfway between the close pair of "blips", and the other extreme midway between the other

pair. This unsymmetrical arrangement makes it possible to identify the direction of the displacement. Hence the phase angle between the force and the displacement was obtained.

The hydrogen bubble technique was used for flow visualization. This technique, which utilizes bubbles generated by the electrolysis of water, has been used by Geller (Ref. 26); Clutter, Smith and Brazier (Ref. 27); Schraub, et. al. (Ref. 28); and Friberg (Ref. 29). As shown by previous experience, it is best suited in the speed range of approximately 1 in/sec to 1 ft/sec. The generating probe was the same as described previously in Ref. 28. Sodium chloride was added to the water as an electrolyte to speed up the generation of hydrogen bubbles which had a tendency to disperse at about $2 \sim 3$ diameters behind the model (depending on the velocity).

II.2 MEASUREMENTS

II.2.1 Damping

In interpreting the flow visualization studies, to be described later in this section, it is important to know when the hydrodynamic forces are driving the oscillating cylinder and when they are damping the motion. By measuring the instantaneous hydrodynamic force on and the displacement of the cylinder simultaneously, it is possible to determine the sign and magnitude of the damping coefficient.

The relationship of the phase angle ϕ (between force and displacement) to the coefficient of damping and apparent mass of the immersed cylinder is needed for the interpretation of the data, and it can be derived once F_a is assumed to have the form of Eq. (1).

Since it was observed that the F_a -signal was a fairly clean sinusoid, it may be accurately approximated by

$$F_a = f_a \sin \omega t \tag{2}$$

When the cylinder is forced into a sinusoidal motion, its displacement may be expressed by

$$y = A \sin (\omega t + \phi) \tag{3}$$

Substituting Eqs. (2) and (3) into (1), one obtains, after some manipulations

$$\phi = \tan^{-1} \frac{c_a}{m_a \omega} \tag{4}$$

Thus, ϕ is also a measure of the damping due to the flow. By estimating m_a and knowing ω and ϕ, an approximate value of c_a may be calculated, if desired. As $|c_a|$ is appreciably smaller than $m_a \omega$ i.e., damping forces are small compared to forces due to the virtual mass for sizable amplitude, ϕ will be small. To improve the accuracy of measuring the point A_0 (the amplitude of oscillations where $c_a = 0$), one can artificially reduce m_a by placing small masses on the dummy cylinder and thus canceling part of the inertia of the apparent mass as well as that of the cylinder. Let the added mass be γm_a (where $\gamma < 1$), then

$$\phi' = \tan^{-1} \frac{c_a}{(1-\gamma) m_a \omega} \tag{5}$$

Equation (5) was qualitatively verified by experiments in which γ was varied. Although the angle ϕ' changes faster than ϕ, the $\phi' = 0$ and $\phi = 0$ points share the same A_0 since $c_a(A_0) = 0$ does not depend on m_a.

Results of the phase angle measurements are shown in Fig. 6. For these tests, the following procedure was followed: the natural frequency of the pendulum and the free stream velocity were fixed, thus fixing also the reduced frequency. The forced amplitude was varied, and the ϕ vs. A data were taken. When the excitation was shut-off, the motion would die out or would stabilize at some noticeable amplitude, depending on the closeness of the reduced frequency to the Strouhal number. In the tests, reduced frequencies were varied over a range of approximately 0.15 to 0.29. Free oscillations (steady oscillations without external applied forces) were observed at reduced frequencies of about 0.20 to 0.22.

Figure 6c shows data taken during two runs. In one run the pendulum was forced to oscillate at fixed amplitude while in the second run it swung freely so that the plotted amplitude is an instantaneous value. All data exhibit one common feature. When the amplitude increases, the phase angle ϕ approaches asymptotically 90° (the maximum damping).

This is as expected, because for a large amplitude oscillation (i.e., of the order of the diameter) the transverse velocity is large compared with the free stream velocity and the hydrodynamic resistance to transverse motion becomes a dominant force.

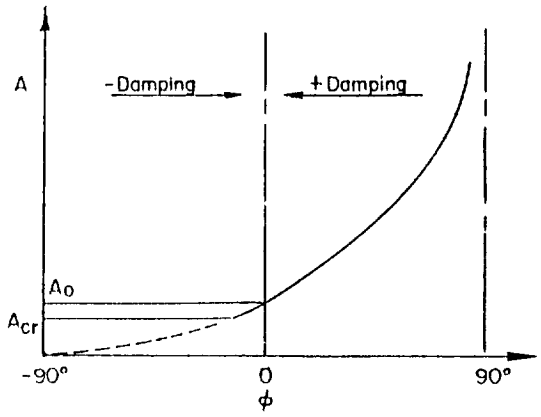

Sketch C

The results of the phase angle measurement can be summarized as follows:

(1) The force is essentially sinusoidal.

(2) Free oscillations are observed at reduced frequencies of approximately 0.20 to 0.22.

(3) The magnitude of the force increases with increasing amplitude.

(4) At the same reduced frequency range (.20 to .22), the angle ϕ is directed towards (-90°) and (+90°) for the low and high amplitude oscillations, respectively.

(5) With the reduced frequency in this range the constant amplitude of the free oscillations, A_{cr}, indicates the neutrally-stable condition (see Sketch C). For $A > A_{cr}$, the motion would damp when the excitation force is released, with the amplitude A decreasing toward the stable value A_{cr}. For $A < A_{cr}$, the motion would build up when the constraint is removed, with the amplitude increasing toward A_{cr}. Structural damping caused the amplitude A_{cr} of the free oscillation to be a little smaller than the amplitude at $\phi = 0$. In other words, after the hydrodynamic forces were neutrally damped (phase angle $\phi = 0$) the free-swinging pendulum would oscillate at decreasing amplitudes until the negative hydrodynamic damping would just compensate for the structural damping at amplitude A_{cr}.

(6) It is significant that the amplitude near $\phi = 0$ was nearly the same over the reduced frequency range of .20 to .22. The Strouhal force apparently "locks in" to the frequency of the motion in this range. This phenomenon has also been observed by Meier-Windhorst and Bishop and Hassan.

II.2.2 Lift and Drag

II.2.2.1 Stationary Cylinder

The strain gage force measurements provided lift (force normal to stream direction) as well as phase information. Furthermore, the support could be rotated by 90° to give the force in the drag direction. Because of gap and free surface effects, the force data can not be considered quantitatively accurate, but would prove useful as a guide in the formation of analytical models.

On the stationary cylinder, the amplitude of the sinusoidally varying two-dimensional lift coefficient, C_ℓ (based on the cylinder diameter and free stream water depth), was found to be nearly constant (about .58) in the Reynolds number range from 4.8×10^3 to 7×10^3 (see Fig. 7). At higher Reynolds numbers (up to 10^4) the lift amplitude decreased, contrary to the trend observed by other investigators (Refs. 8 and 16, for example). Variations in the gap width between the bottom of the channel and the cylinder affected the C_ℓ measurements. As the gap was varied from about .005 inches to .015 inches, the oscillating lift force decreased. The change was not sufficient to account for the total decrease in C_ℓ. However, at the higher water velocities, the water surfaces rose in front of the model and fell below the free stream level toward the rear as shown in Sketch D

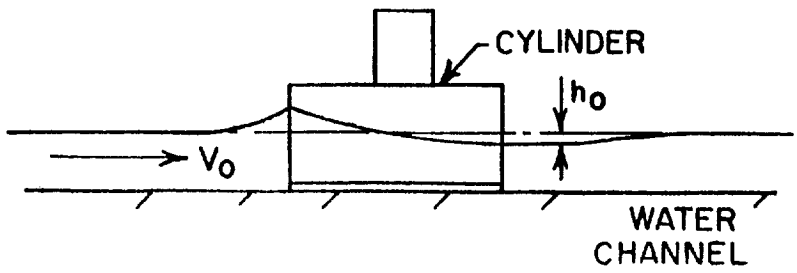

Sketch D

This phenomenon was first easily observable at $Re \simeq 7 \times 10^3$, and the condition was increasingly pronounced at higher Reynolds numbers and correspondingly higher velocities. The change of level, h_o, increased to an estimated 30 percent of the free stream water depth at $Re \simeq 10^4$. When a plexiglas sheet was placed on the water surface, the drop of C_L was considerably slower, from about 0.58 to 0.4 in the Reynolds number range of approximately 7×10^3 to 1.1×10^4. However, the discrepancy of the downward trend as compared with Keefe's result can not be explained with either the gap or the surface effects. It may conceivably be a boundary layer effect since the water was so shallow.

The drag on a stationary cylinder was also measured for comparison with existing data. The drag coefficient C_D, was approximately 1.0 in the Reynolds number range of about 6×10^3 to 1.2×10^4 as shown in Fig. 8. At low flow velocities, a dam was placed well downstream of the model to maintain the water depth in the channel. It did not significantly affect the drag coefficient, but it may have influenced the lift. The value of the drag coefficient is in agreement generally with other measurements on circular cylinders. Although the drag fluctuates slightly (at twice the Strouhal frequency), the alternating component is not a significant fraction of the steady drag force.

II.2.2.2 Oscillating Cylinder

During the measurements of amplitude against phase angle, the magnitude of the lift force on the oscillating cylinder was observed to increase with amplitude of oscillation. This result is in agreement with that obtained by Bishop and Hassan. The measurements have not been analyzed further since they are only qualitatively reliable.

II.3 FLOW VISUALIZATION STUDIES

II.3.1 Wake Behind Stationary Cylinder

From wake observations an analytical model of the flow field about an oscillating cylinder was to be formulated. Therefore the studies centered on the development and trajectories of concentrated vortices appearing in the wake of the cylinder. The flow about the stationary cylinder

was examined first to form a basis for comparison with the oscillatory case. The hydrogen bubble technique, described previously, was used to make visible streaklines in the flow. Still and motion-picture photographs of these lines provided the data from which vortex trajectories were deduced.

The vortex positions were measured from film frames taken at 1/16 second intervals (Fig. 9). The velocity was such that the period for shedding was approximately 9/8 second and thus, 10 consecutive points constituted half a period.

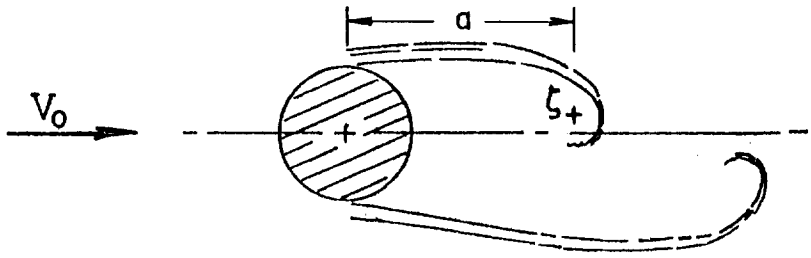

Sketch E

The vortex position ζ was defined as the center of concentration of vorticity near the end of the shear layer emanating from the cylinder surface (see Sketch E). This is somewhat arbitrary because one may argue that ζ can be anywhere inside the concave streakline. However, qualitative results are needed for the formulation of the physical model and this definition will, it is believed, provide an adequate picture of the flow field. With this definition, the vortex first appeared about one diameter behind the cylinder. The vortex, gaining strength as it drifted downstream, was not strong enough to collect enough bubbles so as to be visible before this point. Beyond this point, it moved toward the centerline. After travelling downstream along the centerline for a short distance, it appeared to separate from the feeding sheet. Finally it seemed to move away from the centerline as it drifted further downstream. Figure 9 shows the vortex path on one side. There is a similar path on the opposite side, but with the timings half a period apart.

From observations, the vortex distance (see Sketch E) when it first appeared was a function of velocity. The distance a_o decreased with increasing velocity.

A movement of the separation point associated with the vortex shedding phenomenon was also observed. Again, the separation point was not well defined.

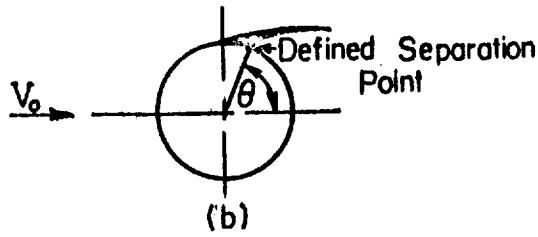

Sketch F

It was chosen, for convenience, to be the point closest to the wake in the bubble region (see Sketch F). As the vortex appeared and started to move toward the centerline, the separation point began to move rearward from about $\theta = 90°$ to $\theta = 60°$ approximately. When the vortex reached the center and drifted downstream, the separation point appeared to be stationary. After the discharge of the vortex, the separation point started to move forward toward $\theta = 90°$, under the influence of the vortex from the other side of the cylinder.

II.3.2 Wake Behind Oscillating Cylinder

When the cylinder oscillated transverse to the stream, the resulting flow field was observed to change considerably. However, many distinct features appeared there which were also seen in the flow field about a stationary cylinder (and discussed in the previous section).

The flow field behind an oscillating cylinder was photographed by a movie camera. Figure 10 presents selected frames from the movies. The reduced frequency was approximately .21, and the relation between damping and phase angle corresponds to that shown in Fig. 6c. In these three sets of photographs, all parameters but the amplitude were kept constant. In each set, the middle photograph corresponds to the median position of the cylinder, while the two end photographs correspond to the extremities of cylinder travel. In (a), the amplitude was small (about 0.2D) corresponding to negative hydrodynamic damping. The wake

looked much like that of the stationary cylinder. In (b), the amplitude was 0.5D, the case of nearly zero damping. Since the frequency was 0.78 cps and the velocity was about 5.7 in/sec, the transverse velocity had an amplitude of 3.5 in/sec which was comparable to the free-stream velocity. One notes significant lateral movement of the vortex in these photographs. In (c), the case of a forced oscillation with a large amplitude (0.7D) and large hydrodynamic damping is depicted; it shows a continuation of the trend from (a) to (b). In this set, the vortex first appeared closer to the cylinder than before. This observation was also made in the study of the stationary case with increasing stream velocity. However, the increase of transverse velocity also forced the hydrogen bubbles to disperse earlier than before and the paths of the vortices could be followed for a downstream distance of only one diameter.

The vortex position behind an oscillating cylinder is presented in Fig. 11 as a function of time, at intervals of 1/12 sec for the high amplitude case. The instantaneous cylinder lateral position is included. In each case, the location of the vortex is relative to the cylinder possessing the same index, i.e., vortex labeled 1 means it is to be considered with cylinder position 1, etc. Arrows at the center indicate directions of motion.

Position 5 corresponds nearly to the location of the clockwise vortex when it was first noted. The vortex had its origin at an earlier time, say at 1. It is interesting to note this position with respect to the cylinder 5, considering the relative wind direction at that time. Instantaneously, the pattern looks like that of the stationary cylinder when the vortex first appeared. At later times, the vortex moves towards the centerline, as in positions 6, 7, 8. Although the path of the vortex with respect to the cylinder and the instantaneous relative wind direction does not follow exactly the trajectory of the stationary case, the amplitude of the vortex motion on this quasi-steady basis is about the same as for the stationary case. The positions 9, 10, 11 were obtained from the observed locations 1a, 2a, etc. of the alternate (counterclockwise) vortex emanating from the other side of the cylinder. Postion 8 of the top vortex corresponds nearly to position 1a of the lower vortex.

The trajectory of the vortex shed from side A is shown in Fig. 11b. The cylinder is fixed in the stream direction in this case, but when the vortex has traveled from position 5 to 5a, the cylinder has moved down to its lowest position. The trajectory of the counterclockwise vortex from side B can be drawn as the image of that from side A about the motion centerline. Both trajectories cross the centerline at a fixed downstream point, but of course, at different times (half a period apart). In comparing these trajectories with those drawn in Ref. 6, one finds disagreement for positions 6 and beyond. As far as it can be determined from Ref. 6, Meier-Windhorst observed the vortex movement for times corresponding to earlier positions 1-5, and extrapolated on these results for later positions.

The movement of the separation point in the oscillating cases was observed. Let t_1 denote the instant when the cylinder was at its median position and travelling downward as seen in Fig. 11 (near position 5); the cylinder crossed the same position travelling upward half a period later. The separation point on side A moved from a position ahead of A ($\theta > 90°$) at time t_1 to a position nearer to the rear stagnation point ($\theta < 90°$) in half a period. This is expected, if one considers the direction of the stream relative to an observer on the cylinder. The separation point indicated for position 5 in Fig. 11a illustrates this situation. The quasi-steady motion of the separation point is then similar (but not identical) to its motion on the stationary cylinder.

II.3.3 The Umbilical Tower Representation

A launch vehicle is usually accompanied by its umbilical tower which may influence the flow field and thus the forces which cause free oscillations. Generally, the towers have complicated cross-sections. For the present qualitative study, simple circular towers were investigated. The three basic parameters, describing a simulated tower are its diameter D', the angular position θ and the separation ℓ with respect to the model (see Sketch G). All lengths are nondimensionalized with respect to the diameter of the model, D .

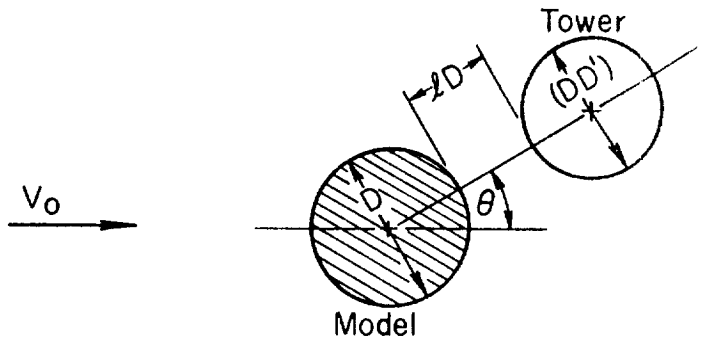

Sketch G

Due to the symmetry of the configuration, it was sufficient to study only half the range of θ (from 0 to π). The free stream velocity was about 6 in/sec ($Re \simeq 6 \times 10^3$, based on the model diameter) and the Strouhal frequency for the model was approximately 0.9 cycle/sec which was the asymptotic value for vanishingly small interference (corresponding to $\ell \to \infty$ or $D' \to 0$). The diameter of the model was 1.5 inch, and, for practical considerations, the ranges for ℓ and D' were restricted as follows:

$$0 \leq \ell \leq 2$$

$$D' = 1.00,\ 0.83,\ 0.50$$

At $\theta = 0$, the influence of the tower, which was weighted by its disturbance on the alternate vortex shedding pattern behind the model, was most significant. For $D' = 1$, no vortex shedding was observed for $\ell < 2$ and the flow field consisted of one straight trailing wake. At $\ell \simeq 2$, a small oscillatory motion was noted in the wake. For $D' = 1/2$, the alternate vortex shedding appeared behind the tower for the range $\ell = 0$ to $\ell \simeq 0.7$, with frequency increasing toward the asymptotic value. Between $\ell \simeq 0.7$ and $\ell \simeq 1.7$, the vortex disappeared, since the tower occupied the position where the vortex would have been. However, for $\ell >$ approximately 1.7, the alternate vortex shedding was noted once more between the model and the tower, with frequencies closer than before to the asymptotic value.

At $\theta = \pi/4$, the influence appeared to be different. Alternate vortex shedding was observed behind the tower, but not the model. At $\mathcal{D}' = 0.5$ and $\mathcal{L} \simeq 2$, the oscillatory motion of the wake behind the model appeared. Generally, the flow field is as shown in Fig. 12.

At $\theta = \pi/2$, strong vortex shedding was generated when the tower touched the model ($\mathcal{L} = 0$) because the two structures formed effectively an equivalent ellipse (Fig. 13). As shown in Fig. 14 the maximum frequency was reached at $\mathcal{L} \simeq 0.7$ and then decreased toward the asymptotic value as the interaction faded away. The fluid which was accelerated through the gap, was subjected to the vortex sheddings from both the model and the tower. When $\mathcal{D}' = 1$, continuous vortex shedding was observed. However, when the diameter of the model and the tower were different ($\mathcal{D}' \neq 1$), the interaction of the two different vortex shedding frequencies caused the vortex behind the model to diminish and reappear in a periodic manner. At $\theta = 3\pi/4$, the vortex shedding was observed only behind the model and the frequency was generally below the asymptotic value (Fig. 15). The flow field was similar to the case of $\theta = \pi/4$.

At $\theta = \pi$, the flow field configuration was similar to that for $\theta = 0$ and a straight wake was observed to trail behind the model. For $\mathcal{D}' = 0.5$ and $\mathcal{L} >$ approximately 1, the wake started to have an oscillatory motion.

SECTION III

ANALYTICAL MODELS

III.1 GENERAL

This section describes the formulation of two simple mathematical models of the flow field and calculations of the aerodynamic forces on a stationary circular cylinder exposed to a steady free stream. It represents the initial effort towards the ultimate objective of deriving a method capable of predicting adequately the forces on an oscillating cylinder. Means of extending the formulation to small amplitude oscillations are also offered and briefly discussed.

The analyses are based on the following important assumption:

The flow field is potential, but possesses singularities at vortex points and cuts along the so-called feeding sheets (i.e., the infinitesimally thin, free shear layers) which join the cylinder with the two nearest vortices, one on each side of the cylinder.

Previous investigators have adopted potential flow models for the separated flow behind circular cylinders with various degrees of success. Bryson (Ref. 22) treats the case of the lift on a slender cone at high angles of attack in the subsonic to the moderately supersonic velocity range, by analyzing the symmetric vortex separation on the leeward sides of such bodies. His analysis utilizes the "lumped vorticity" approximation of Edwards and Hill (Refs. 30, 31). In a recent report (Ref. 23), Ujihara discussed the initial phases of the wake development behind a circular cylinder set into motion impulsively. This problem was also treated by Bryson who used a different model. Ujihara's calculations could, in principle, be extended for longer periods of time (at the expense of much increased computer time) and be interpreted as results for the "steady" periodic vortex shedding problem.

In Bryson's model, vorticity is released by the boundary layer to the wake through feeding sheets which are assumed attached to the

cylinder at the fixed points $\theta = \theta_0$ and $\theta = \pi - \theta_0$ (see Fig. 16a). These points are stagnation points. Their selection is based on observations and trial analyses. A further simplifying assumption in this model is that all the shed vorticity is carried instantaneously from the boundary layer to a "center of concentration" which is taken to be the location of the single vortex representing the entire layer. In reality, of course, the vorticity is distributed all along the shear layer, but, as brought out by the elaborate calculations of other investigators, with heavier concentration near the end of the vortex sheet, particularly when it is removed from the cylinder. In the present case of antisymmetric shedding, each vortex is assumed to be fully developed and to break away from its feeding sheet after a certain period following its inception, leaving the boundary layer to supply a newly-formed vortex near the cylinder. This period is related to the well-known Strouhal number.

This simplified representation of the shear layer requires that there be zero force exerted by the flow on the attached vortex and its feeding sheet. Two expressions imposing this requirement for the two attached vortices*, along with certain kinematic relations describing the locations of the stagnation points and the induced velocities at the vortices, constitute the basic equations of the problem.

An objection to this model is that nowhere in the analysis is the rate of vorticity generation related explicitly to the boundary layer variables. It is dependent in a somewhat indirect manner, in that the stagnation points chosen following experimental observations are influenced by the boundary layer development.

In Ujihara's model, the shear layer is replaced not by a single vortex with an attendant feeding sheet but with a large number of very small discrete vortices shed at very short and equal intervals. The rates and strengths of these small vortices are somewhat dependent on the choice of the feeding point location. Ujihara takes this location to

*In the symmetric problem of Ref. 22, only one equation need be considered.

coincide with the first minimum pressure point (which varies with time) aft of the forward stagnation point. The rate of vorticity generation depends on the fluid velocity at the edge of the boundary layer and at the "feeding point".

III.2 ANALYTICAL MODEL I

The model first considered and tested follows that of Bryson, but with modifications to extend to the antisymmetric problem. Figure 16b depicts the situation of a stationary cylinder in a simplified flow field. The center of the cylinder is at the origin of the complex coordinate system $\zeta = y + iz$, and the free stream velocity V_0 is directed along the iz-axis. Γ_1 and Γ_2 represent the strengths of the two nearby vortices with feeding sheet attachment points at θ_0 and $\pi - \theta_0$ respectively. Γ_3 and Γ_4 are detached vortices which constitute the rest of the antisymmetric wake. The boundary condition of zero velocity normal to the cylinder is met by introducing image vortices inside the cylinder.

A more complete though still idealized picture would have the antisymmetric array of vortices continuing to infinity (with corresponding image vortices), with a center vortex to account for the "unsteady conditions" at the beginning of the motion. From practical considerations, however, it is necessary to limit the analyses to a few of the vortices. This is not a severe limitation in the case of the lift force predictions, for the effects of the neglected vortices can be adequately approximated by those due to a single vortex Γ_c at "$\zeta_c \to i\infty$" (and its image at "$\zeta_{ci} \to 0$"). Some caution must be exercised in the manner of effecting this approximation. The inclusion of the image vortex at "$\zeta_{ci} \to 0$" is a necessity even though it has no effect on the boundary condition; without Γ_{ci}, the situation would be quite different with the inclusion of an even number of wake vortices from that with an odd number. This point will be clarified in subsequent discussions for the case with four outside vortices.

Since the flow is periodic (of period t_p, say), the mathematical models should be completely antisymmetric at the end of the half period. Sketch H shows the position of the three vortices at selected times.

In (a), the situation is for time $t = t_b$ which corresponds to the instant just after Γ_3 is fully developed and breaks away from its feeding sheet to allow growth of Γ_1. Just before the end of the half period, i.e., $t = \frac{1}{2} t_p^- + t_b$, the vortices are in the positions indicated in (c). At this time, Γ_3 is sufficiently removed to be "switched" to the far wake (which is approximated by Γ_c). At time $t = \frac{1}{2} t_p^+ + t_b$, the switching is carried out, and the resultant pattern is illustrated in (d). This is acceptable if Γ_c is taken to be equal to $\frac{1}{2}\Gamma_3$. For then Γ_3 and Γ_c (which are of opposite direction) combine to give a new Γ_c in the opposite direction; and their images also combine at the center to yield a new Γ_{cc} of opposite direction*. The conditions in (d) are completely antisymmetric with respect to those in (a).

The two vortices Γ_1 and Γ_2 are <u>unequal</u> in magnitude and vary with time, being constantly strengthened by the feeding sheets emanating from the stagnation points ζ_{01} and $\zeta_{02} (= -\bar{\zeta}_{01})$**. Γ_3 (and beyond) are fully developed and detached, and are therefore of constant strength.

The period of the oscillatory flow is easily determined in terms of the Strouhal number (St) for the stationary cylinder***. For practical purposes, St may be taken equal to 0.2 in the subcritical Reynolds number range of interest. Since $St = \frac{f_s (2a)}{V_0}$, where a is the cylinder radius and f_s the vortex shedding frequency, the period t_p turns out to be

$$t_p = \frac{1}{f_s} = \frac{2a}{V_0 (St)} = \left(\frac{10a}{V_0}\right) \qquad (6)$$

The complex velocity potential w receives contributions from (a) a doublet at the origin and the free stream to simulate the flow about a cylinder, (b) the four vortices Γ_1, Γ_2, Γ_3 and Γ_c, and (c) the image vortices Γ_{1i}, Γ_{2i}, Γ_{3i} and Γ_{ci}. This potential at any point ζ is

---

* A five-vortex approximation, i.e., with a Γ_4 included, would require that the vortices Γ_c and Γ_{cc} be of the same strength as in the four-vortex approximation but of opposite sense.

** A bar over a complex variable indicates its conjugate.

*** For the oscillating cylinder, with a reduced frequency of motion sufficiently close to the Strouhal number, the period would be related to that reduced frequency.

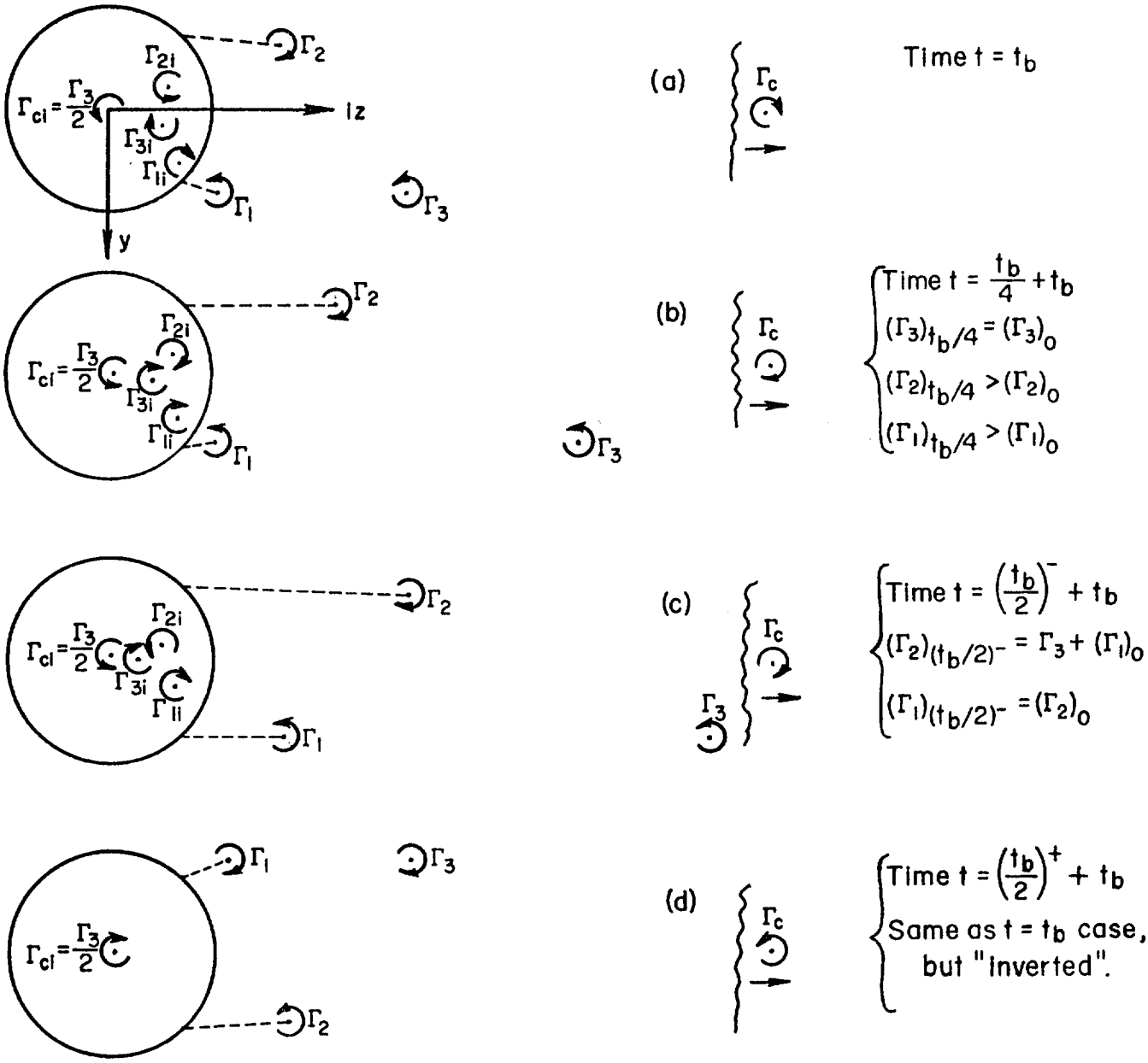
Γ_2
Γ_{2i}
$\Gamma_{ci}=\frac{\Gamma_3}{2}$
Γ_{3i}
Γ_{1i}
Γ_1
Γ_3
z
y
(a)
Γ_c
Time $t = t_b$
(b)
Γ_c
Time $t = \frac{t_b}{4} + t_b$
$(\Gamma_3)_{t_b/4} = (\Gamma_3)_0$
$(\Gamma_2)_{t_b/4} > (\Gamma_2)_0$
$(\Gamma_1)_{t_b/4} > (\Gamma_1)_0$
(c)
Γ_c
Γ_3
Time $t = \left(\frac{t_b}{2}\right)^- + t_b$
$(\Gamma_2)_{(t_b/2)^-} = \Gamma_3 + (\Gamma_1)_0$
$(\Gamma_1)_{(t_b/2)^-} = (\Gamma_2)_0$
(d)
Γ_c
Time $t = \left(\frac{t_b}{2}\right)^+ + t_b$
Same as $t = t_b$ case, but "inverted".

Sketch H

expressed in terms of the locations $\zeta_1, \cdots \zeta_c$ of the four vortices as follows:

$$w = \phi + i\psi = -iV_0\left(\zeta - \frac{a^2}{\zeta}\right) - i\frac{\Gamma_c}{2\pi}\ln\left(\zeta - \frac{a^2}{\zeta_c}\right) + i\sum_{s=1}^{3}(-1)^s \ln\left[\frac{(\zeta-\zeta_s)}{\left(\zeta - \frac{a^2}{\zeta_s}\right)}\right] + i\frac{\Gamma_c}{2\pi}\ln(\zeta - \zeta_c) \tag{7}$$

The dimensionless complex velocity, $\frac{1}{V_0}(u - iv)$, follows immediately from (7), noting that the Γ_c -vortex is far removed and $|\zeta_c| \to \infty$

$$\frac{1}{V_0}(u - iv) = \frac{1}{V_0}\frac{dw}{d\zeta} = -i(1 + \eta^{-2}) - i\lambda_c(\eta^{-1}) + i\sum_{s=1}^{3}(-1)^s\lambda_s\left[\frac{1}{\eta - \eta_s} - \frac{1}{\eta - \frac{1}{\bar{\eta}_s}}\right] \tag{8}$$

In the last expression, the dimensionless variables

$$\lambda_s = \frac{\Gamma_s}{2\pi a V_0} \quad \text{and} \quad \eta = \frac{\zeta}{a} \tag{9a,b}$$

have been introduced for convenience. Since $\eta_0 \left(= \frac{\zeta_0}{a}\right)$ and $-\bar{\eta}_0$ are stagnation points, $\frac{1}{V_0}(u - iv)$ must be zero there; and Eq. (8) yields after some algebra, realizing that $\eta_0\bar{\eta}_0 = 1$,

$$\left\{\eta_0 + \bar{\eta}_0\right\} = -\lambda_c + \sum_{s=1}^{3}(-1)^s\lambda_s\left\{\frac{\eta_0}{\eta_0 - \eta_s} - \frac{\eta_0}{\eta_0 - \frac{1}{\bar{\eta}_s}}\right\}$$

$$\left\{\eta_0 + \bar{\eta}_0\right\} = \lambda_c - \sum_{s=1}^{3}(-1)^s\lambda_s\left\{\frac{\bar{\eta}_0}{\bar{\eta}_0 + \eta_s} - \frac{\bar{\eta}_0}{\bar{\eta}_0 + \frac{1}{\bar{\eta}_s}}\right\} \tag{10a,b}$$

Equations (10a, b) constitute a set of two <u>real</u> equations, because the quantities in the curly brackets are all real, as evidenced by the identities

$$\eta_0 + \bar{\eta}_0 = 2\,Re(\eta_0) = 2\cos\theta_0 \equiv E$$

$$\frac{\eta_0}{\eta_0 - \eta_s} - \frac{\eta_0}{\eta_0 - \frac{1}{\bar{\eta}_s}} = 2\,Re\left(\frac{\eta_0}{\eta_0 - \eta_s}\right) - 1 \equiv A_s \qquad (11a,b,c)$$

$$\frac{\bar{\eta}_0}{\bar{\eta}_0 + \eta_s} - \frac{\bar{\eta}_0}{\bar{\eta}_0 + \frac{1}{\bar{\eta}_s}} = 2\,Re\left(\frac{\eta_0}{\eta_0 + \bar{\eta}_s}\right) - 1 \equiv B_s$$

The strengths λ_1, and λ_2 are related to λ_3 and λ_c in terms of the position variables $\eta_0, \cdots \eta_3$; according to Eqs. (10a,b),

$$\lambda_1 = \frac{-E(A_2 + B_2) + \lambda_c (A_2 - B_2) + \lambda_3 (A_2 B_3 - A_3 B_2)}{A_1 B_2 - A_2 B_1} \equiv \frac{N_1}{D}$$

$$\lambda_2 = \frac{-E(A_1 + B_1) + \lambda_c (A_1 - B_1) + \lambda_3 (A_1 B_3 - A_3 B_1)}{A_1 B_2 - A_2 B_1} \equiv \frac{N_2}{D} \qquad (12a,b)$$

The velocities $V_0 Q_i\ (=(u+iv)_i)$ of vortices 1 and 2, excluding the "infinite self-induced velocities"*, are obtained directly as the conjugates of $\frac{dw}{d\zeta}$ from Eq. (8):

$$Q_i = i\left\{(1 + \bar{\eta}_i^{-2}) + \lambda_c (\bar{\eta}_i^{-1}) + \sum_{s=1}^{3}{}' (-1)^{s+1} \lambda_s \left(\frac{1}{\bar{\eta}_i - \bar{\eta}_s}\right) + \sum_{s=1}^{3} (-1)^s \lambda_s \left(\frac{1}{\bar{\eta}_i - \frac{1}{\eta_s}}\right)\right\};\ i = 1,2 \qquad (13)$$

The prime in $(\sum')$ indicates that the term $i = s$ is to be omitted in the summation. The condition of zero net force on the vortex and its connecting sheet yields the relations (see Ref. 22)

$$\eta_1' + (\eta_1 - \eta_0)\frac{\lambda_1'}{\lambda_1} = Q_1\,;\quad \eta_2' + (\eta_2 + \bar{\eta}_0)\frac{\lambda_2'}{\lambda_2} = Q_2 \qquad (14a,b)$$

* These velocities should be excluded, since the velocity at the center of the vortex due to itself should be zero.

where $(\ )'$ denotes differentiation with respect to the dimensionless time $\tau = \frac{V_0 t}{a}$. Equations (14a, b) are two complex (or equivalently four real) simultaneous, nonlinear, first-order differential equations. Coupled with Eqs. (12a, b), they form a set of six equations which are to be solved for the strengths λ_1, λ_2 and the positions $\eta_1 = \eta_{1r} + i\eta_{1i}$, $\eta_2 = \eta_{2r} + i\eta_{2i}$ of the growing vortices as functions of time. How the strength and the position of the third vortex λ_3, and the stagnation points η_0 and $-\bar{\eta}_0$ are introduced in the calculations will be discussed later.

Once the strengths, locations and velocities of all the vortices are determined, the forces acting on the cylinder may be found by summing contributions from the rates of change of the impulse from each pair of vortices (i.e., vortex plus its image)*. The total impulse is given by (see Ref. 22)

$$I = -i\rho \sum_{s=1}^{3} (-1)^s \Gamma_s \left(\zeta_s - \frac{a^2}{\bar{\zeta}_s}\right) + i\rho \Gamma_c \left(\zeta_c - \frac{1}{\bar{\zeta}_c}\right) \qquad (15)$$

and its rate of change by

$$\frac{dI}{dt} = L + iD = -i\rho \sum_{s=1}^{2} (-1)^s \dot{\Gamma}_s \left(\zeta_s - \frac{a^2}{\bar{\zeta}_s}\right) - i\rho \sum_{s=1}^{3} (-1)^s \Gamma_s \left(\dot{\zeta}_s + \frac{a^2}{\bar{\zeta}_s^2}\,\dot{\bar{\zeta}}_s\right)$$
$$- i\rho \Gamma_c \left(\dot{\zeta}_c + \frac{1}{\bar{\zeta}_c^2}\,\dot{\bar{\zeta}}_c\right) \qquad (16)^{**}$$

where $\dot{\zeta}_c$ is the velocity of the vortex representing the wake beyond Γ_3. Taking the lateral force positive in the y-direction, the lift coefficient per unit cylinder length, and based on cylinder diameter, turns out to be (with $\Gamma_c = \frac{\Gamma_3}{2}$)

---

* See Appendix A.

** The conditions that the third vortex is of constant strength, i.e., $\lambda_3' = 0$, and that $|\zeta_c| \to \infty$ are imposed to produce this equation.

$$c_\ell = \frac{L}{(1/2\rho V_0^2)(2a)} = 2\pi\, \mathrm{Im}\left[\sum_{s=1}^{2} (-1)^s \left\{ \lambda_s' \left(\eta_s - \frac{1}{\bar{\eta}_s}\right) + \lambda_s \left(\eta_s' - \frac{1}{\bar{\eta}_s^2}\,\bar{\eta}_s'\right) \right\} + \lambda_3 \left\{ \tfrac{1}{2}\,\eta_c' - \left(\eta_3' - \frac{1}{\bar{\eta}_3^2}\,\bar{\eta}_3'\right) \right\} \right] \qquad (17)$$

A corresponding expression may be written down for the drag (see Appendix A)*.

The strengths, locations and velocities of the vortices are determined in the following manner: When λ_1, λ_2 from Eqs. (12) and their derivatives λ_1', λ_2' are substituted into Eqs. (14a, b), there results a set of four real, simultaneous differential equations. The first two, for example,

$$\eta_{1r}' + (\eta_{1r} - \eta_{0r}) \left\{ \frac{N_1'}{N_1} - \frac{D'}{D} \right\} = Q_{1r}$$

$$\eta_{1i}' + (\eta_{1i} - \eta_{0i}) \left\{ \frac{N_1'}{N_1} - \frac{D'}{D} \right\} = Q_{1i} \qquad (18a, b)$$

are associated with λ_1. To start the numerical integration of these nonlinear equations, the following additional information is required:

(a) The locations of the stagnation points (assumed fixed), η_0, or equivalently θ_0 since $\eta_0 = e^{i\theta_0}$. As stated earlier, the choice of θ_0 is guided by experimental results and trial analyses. To be realistic, θ_0 should be in the range $0 \le \theta_0 \le \frac{\pi}{4}$ rad.

(b) The starting positions of λ_1, λ_2 and λ_3, i.e., η_1, η_2 and η_3 at $\tau = \tau_b$, where τ_b is a suitable starting time.

(c) The strength of the third vortex λ_3.

(d) An expression describing the movements of λ_3 and λ_c. Since λ_3, λ_c remain constant, and the forces on these vortices are

* The error due to the "far wake" approximation (i.e., replacing all vortices beyond Γ_3 by the single vortex at "$i\infty$" of magnitude $\Gamma_c = \frac{\Gamma_3}{2}$ would be much larger in the drag than in the lift, and the drag computed in this manner would be very inaccurate.

zero, the additional conditions of (since $|\eta_c| \to \infty$)

$$\eta_3' = q_3 \; ; \quad \eta_c' = c \tag{19a, b}$$

corresponding to Eqs. (18a, b) may be imposed. This would add four real differential equations to the previously derived four. A simpler alternate to Eq. (19a), which should be adequate and is used here, is to assume a constant velocity $\eta_3' = \eta_{3c}'(\tau = \tau_b) \equiv (\eta_{3c}')_b$ with the result that

$$\eta_3 = (\eta_3)_b + (\eta_{3c}')(\tau - \tau_b) \tag{20}$$

This means that specification of $(\eta_3)_b$ and $(\eta_{3c}')_b$ is sufficient to describe the position of λ_3 at any time. Also, in this analysis, the condition stated by Eq. (19b) has not been imposed. η_c' does not enter into the equations describing the vortex movements, but appears in the force expressions (cf. Eq. (17)). Furthermore, since λ_c and η_c' are both constants, they add only a constant term to the lift; rather than taking $\eta_c' = c$ in the numerical calculations, η_c' is assigned that value which makes c_ℓ have equal magnitudes (but opposite in direction) at times τ_b and $(\tau_b + \frac{1}{2}\tau_p)$.

The solution is started at that time $t_b(\tau = \tau_b)$ just after vortex 3 "breaks away" from its feeding sheet. This time corresponds also to the introduction of vortex 1. Fixing the starting time in this manner is convenient for imposing the antisymmetry conditions at the later time $t_b + \left(\frac{t_p}{2}\right)^-$ (or $\tau = \tau_b + 5^-$). Let subscript b and e denote respectively conditions at $\tau = \tau_b$ and $t = \tau_b + 5^-$. The antisymmetry conditions are then expressed as:

$$(\lambda_1)_e = (\lambda_2)_b \; ; \quad 2\lambda_c = \lambda_3 = \left[(\lambda_2)_e - (\lambda_1)_b\right] \tag{21a, b}$$

$$(\eta_{1r})_e = -(\eta_{2r})_b \; ; \; (\eta_{1c})_e = (\eta_{2c})_b \; ; \; (\eta_{2r})_e = -(\eta_{3r})_b \; ; \; (\eta_{2c})_e = (\eta_{3c})_b \tag{22a-d}$$

$$(\eta_{1r}')_e = -(\eta_{2r}')_b \; ; \; (\eta_{1c})_e = (\eta_{2i})_b \; ; \; (\eta_{2r}')_e = -(\eta_{3r}')_b \; ; \; (\eta_{2i}')_e = (\eta_{3c}')_b \tag{23a-d}$$

All these relations should be satisfied if the flow is to be periodic. This requires an iterative technique wherein certain parameters and initial values, θ_0 , η_{1r} , η_{1i} , η_{2r} , η_{2i} , η_{3r} , η_{3i} , λ_3 , η'_{3r} , η'_{3i} , are adjusted repeatedly to fulfill ultimately the stated conditions.

It should be noted that $(\lambda_1)_0 \neq 0$ in Eq. (19b), i.e., the first vortex starts initially with a finite strength. This also implies that when a vortex breaks away from its feeding sheet, it "returns a small portion of its strength" to the point where it originally started and where a new vortex begins. This fictitious condition must be accepted in the approximation, for λ_1 can be zero only when $\eta_1 = \eta_0$, a result deducible from Eqs. (11) and (12). Bryson points out that the feeding point η_0 is an unstable equilibrium point for the vortex, and that it is necessary to start the numerical integration at a point $(\eta_1)_0$ located a short distance ρ from η_0 and along a preferred direction, namely, at an angle of $\frac{\pi}{6}$ rad. to the downstream tangent to the cylinder at $\theta = \theta_0$, i.e.,

$$(\eta_1)_0 = (\eta_0) + \rho e^{i(\theta_0 - \frac{\pi}{6})}$$

Parallel steps for the present antisymmetric case show that the preferred direction is again as in Bryson's case. Therefore $(\eta_{1r})_0$ and $(\eta_{1i})_0$ may be fixed by choosing the <u>single</u> parameter ρ in the initial conditions.

Certain complications do arise, however, in the numerical procedure. A critical question to be answered is how large should ρ be. If it is too small, it would take λ_1 too long a period to attain any "speed" and proceed downstream to the point of λ_2 at the end of the half period. It cannot be too large either, for then difficulties arise in matching other antisymmetry conditions. This problem is intimately associated with the choice of t_b .

One possible alternative, which has been tried with very limited success, is to start the solution at time $t=0$ (or $\tau=0$) prior to t_b , assuming initial positions $(\eta_{1r})_0, \cdots, (\eta_{3r})_0$. The solution is carried for $0 \leq \tau \leq 7$, a time span somewhat greater than the half period $(\frac{1}{2}\tau_p = 5)$. τ_b is treated as one of the adjustable parameters, variations of which allow satisfaction of the antisymmetry conditions between times τ_b and $\tau_b + 5$. The useful results are then extracted from the solution for $\tau_b \leq \tau \leq \tau_b + 5$.

This sort of iterative technique, with many variables to be adjusted so as to satisfy an equal number of stated conditions, becomes prohibitively long and costly, even with high speed computers. This would be the case even if the initial assumed values of the variables are "reasonably" close to the actual values*. One then inquires as to the possibility of relaxing those antisymmetry conditions which are relatively unimportant for the cylinder lift calculations. Experience indicates that the conditions imposed by Eqs. (21a, b) and (22a, b) are the most important. The remaining conditions can then be checked for "gross errors", especially Eqs. (23a-b) which pertain to the near vortices.

It should be realized however that such a procedure, wherein there are more variables than conditions, leads to nonunique solutions in a strict sense. On the other hand, if the influence of certain of these variables is small, the obtained solution may be sufficiently close to the actual to be acceptable practically, especially if checks on the other conditions reveal no serious errors.

III.3 ANALYTICAL MODEL II

In the previous model, the strengths of the nearby vortices are determined by taking $\zeta = ae^{i\theta_0}$ and $\zeta = ae^{i(\pi-\theta_0)}$ as the stagnation points. The solution turns out to be quite sensitive to the locations of these stagnation points. Experimentally, they are difficult to define for (a) they are not stationary during the cycle, and (b) they are clouded by "large" regions of near-zero velocity.

In Model II, the specification of stagnation points is replaced by the following assumptions:

(a) The nearby vortices are fed at a constant rate.

(b) The feeding points are at two stationary points η_f and $-\bar{\eta}_f$ which are slightly removed from the cylinder. Otherwise the vortex pattern is as in the previous model (see Fig. 16b). Assumption (a)

---

* There is the further consideration that the iteration may diverge with poor initial guesses on θ_0, τ_b, etc.

leads to

$$\frac{d\Gamma_1}{dt} = \frac{d\Gamma_2}{dt} = 2\pi r V_0^2 \tag{24a}$$

where r is a dimensionless rate of vorticity generation. Equation (24a) may be recast into the useful form

$$\frac{d\lambda_1}{d\tau} = \frac{d\lambda_2}{d\tau} = r; \tag{24b}$$

also, one may write for $\lambda_1, \cdots \lambda_c$

$$\lambda_1 = r(\tau + \tau_i); \quad \lambda_2 = r(\tau + \tau_i + 1/2\,\tau_p)$$
$$\lambda_c = 1/2\,\lambda_3 = 1/2\, r\,\tau_p \tag{25a-c}$$

In Eqs. (25a-c), the first vortex starts with a finite strength $\lambda_1 = r\tau_i$ at the point η_f, and after being fully developed, returns this amount to its successor*. The manner of determining τ_i and r will be discussed later. Equations (25a,b) are then the counterparts of Eqs. (12a,b) for Model I, whereas (25c) fixes the final strength of each vortex, removing the necessity of assuming λ_c.

The condition of no net force on each nearby vortex and its feeding sheet leads to the expressions

$$\eta_1' + (\eta_1 - \eta_f)\frac{1}{(\tau + \tau_i)} = Q_1$$
$$\eta_2' + (\eta_2 + \bar{\eta}_f)\frac{1}{\tau + \tau_i + 1/2\,\tau_p} = Q_2 \tag{26a,b}$$

which are considerably simpler in form for solution than the corresponding ones (Eqs. 14a,b) for Model I. The Q_1 and Q_2 are as before (see Eq. 13).

An objection may be raised against Model II. Ujihara's results show that both r and η_f vary considerably during the cycle, whereas they are assumed constant in the above. Whether the r- and η_f-variations are severe enough to effect markedly the total oscillatory lift (particularly

* It is recalled that this artificial condition was also introduced in the Model I analysis.

when viewed over a cycle, rather than at discrete times) cannot be determined at the present. The final evaluation of the proposed model must be made on the basis of comparisons of predicted loads with experiment.

The method of solution of Eqs. (26a, b) is very similar to the previous case, with the added simplifications that: (a) each of the four real equations (26a, b) contains only one derivative and this derivative does not occur in the other equations, (b) the first two of the antisymmetry conditions (Eqs. 21a, b) need no longer be checked, as they are automatically satisfied by the introduction of the assumed forms for λ_1 and λ_2, Eqs. (25a, b). The parameters and initial points that are varied to satisfy the remaining antisymmetry conditions are: r, τ_i, $\eta_{1r}(=\eta_{f_r})$, $\eta_{1i}(=\eta_{f_i})$, η_{2r}, η_{2i}, η_{3r}, η_{3i}, η'_{3r}, η'_{3i} *. There are more variables than conditions, and once more the obtained solutions are not unique. As in the previous case, it would be difficult to satisfy all the conditions of Eqs. (22) and (23); accordingly, only Eqs. (22a, b) and (23a, b) are imposed, as they are deemed to be the most important.

Calculations based on Model I and Model II approximations are now presented to illustrate and to elaborate on some points made earlier.

III.4 NUMERICAL RESULTS

In all calculations presented below, the numerical integration of the differential equations were carried out using sufficiently small increments $\Delta\tau$ of the independent variable. The differential equations were cast into the form

$$\eta'_s(\tau) = f_s\left(\eta_1(\tau), \eta_2(\tau), \cdots, \eta_n(\tau)\right) \qquad (27)^{**}$$

---

* Also η'_c in the calculation of c_ℓ ; the expression for c_ℓ is once more Eq. (17), but with $\lambda_1, \cdots \lambda_c$ given by Eqs. (25a-c).

** In Model I calculations, it is necessary to solve a set of Eqs. (18a, b) to arrive at the form of Eq. (27), because $\mathcal{N}'$ and $\mathcal{D}'$ contain derivatives of η_s . As pointed out earlier, for Model II the corresponding Eqs. (26a, b) are initially of the same form as (27).

and replaced by algebraic relations

$$\eta_s'(\tau_i) = f_s(\eta_1(\tau_i), \eta_2(\tau_i), \cdots, \eta_n(\tau_i))$$

$$\eta_s(\tau_{i+1}) = \eta_s(\tau_i) + \left[\eta_s'(\tau_i)\right]\Delta\tau$$

The adequacy of this procedure was checked by taking successively smaller values of $\Delta\tau$. For all practical purposes, the same numerical results were obtained once $\Delta\tau$ was made equal to or less than $\rho/2$.

III.4.1 Model I Calculations

To establish a reasonable set of initial values for the iterative scheme, a few trial runs were made starting with various values of the initial parameters. The run which appeared closest to satisfying the antisymmetry conditions started out with

$$\theta_0 = 35°,\ \rho = 0.03,\ \tau_b = 0.2$$

$$(\eta_{2r} + i\eta_{2i})_0 = -1.0 + 0.9i,\ (\eta_{3r} + i\eta_{3i})_0 = 1.0 + 2.8i$$

$$(\eta_{3r}' + i\eta_{3i}')_0 = \text{constant} = 0.5i;\ \lambda_c = (\lambda_3/2) = 0.65$$

It yielded the ratios

$$r_1 \equiv \frac{(\lambda_1)_e}{(\lambda_2)_b} = 0.948,\quad r_2 \equiv \frac{(\lambda_2)_e - (\lambda_1)_b}{\lambda_3} = 1.045$$

$$r_3 \equiv \frac{(\eta_{1r})_e}{(\eta_{2r})_b} = 0.942,\quad r_4 \equiv \frac{(\eta_{1i})_e}{(\eta_{2i})_b} = 1.09$$

The quantities $r_1, \cdots r_4$ should have assumed the value of unity if the most important antisymmetry conditions Eqs. (22a, b; 23a, b) were to be satisfied exactly. Taking this as the base case, additional series of runs were made; in each series, all but one of the parameters were held fixed. For instance, by varying λ_c, the quantities $\frac{\partial r_n}{\partial \lambda_c}$ (n = 1, 2, 3, 4) could be

determined. Hopefully, having all these pertinent derivatives $\left(\frac{\partial r_n}{\partial \theta}, \ldots, \frac{\partial r_n}{\partial \lambda_c}\right)$, the initial parameters could be so readjusted as to bring the ratios closer to unity. This was found to be unsuccessful, because any of the initial parameters, when varied a small amount in one direction, had beneficial effects on some ratios, and detrimental effects on the rest.

The main difficulty seemed to arise from the choice of τ_b . The ratios were found to be strongly dependent on this parameter. The derivatives $\frac{\partial r_n}{\partial \tau_b}$ were also noted to be sensitive to τ_b , and were not easily obtainable. The original program allowed steps of τ_b of 0.1 or above only. For this reason, an iterative program was written in which τ_b could be varied at will; unfortunately, to this date, the latter program has not produced a convergent iteration and no meaningful numerical results based on the Model I approximation are available.

III.4.2 Model II Calculations

Model I – calculations have not been pursued further because of their heavy demand in machine time. Also, the simpler calculations based on Model II have shown more promise.

The following tables describe two sets of solutions according to the latter method.

Initial Parameters	$(\eta_{1r})_0$	$(\eta_{1i})_0$	$(\eta_{2r})_0$	$(\eta_{2i})_0$	$(\eta_{3r})_0$	$(\eta_{3i})_0$	$(\eta'_{3r})_0$	$(\eta'_{3i})_0$
Set 1	1.00	0.158	-0.5	1.80	0.941	4.013	0.	0.7057
Set 2	0.846	0.592	-0.367	2.30	0.740	5.210	0.	0.697

Other Parameters	$\bar{F}$	τ_i	τ_b	Δt	η'_{ci}	Remarks
Set 1	0.080	0.20	0.50	0.025	0.584	a. Lower values of $\Delta\tau$ did not change results. b. η'_{ci} so chosen as to make c_ℓ have equal magnitudes for times τ_b and $\tau_b + 5.0$.
Set 2	0.073	0.144	0.50	0.025	0.460	

	$r_3 = -\frac{(\eta_{1r})_e}{(\eta_{2r})_b}$	$r_4 = \frac{(\eta_{1i})_e}{(\eta_{2i})_b}$	$r_5 = -\frac{(\eta'_{1r})_e}{(\eta'_{2r})_b}$	$r_6 = \frac{(\eta'_{1i})_e}{(\eta'_{2i})_b}$	Remarks
Set 1	1.000	1.000	0.999	1.000	Parameters varied to bring $r_3, \ldots r_6$ inc. close to unity
Set 2	1.000	1.000	1.001	1.000	

	$r_7 = -\frac{(\eta_{2r})_e}{(\eta_{3r})_b}$	$r_8 = \frac{(\eta_{2i})_e}{(\eta_{3i})_b}$	$(\eta'_{2r})_e$	$r_9 = \frac{(\eta'_{2i})_e}{(\eta_{3i})_b}$	Remarks
Set 1	0.308	0.920	-0.066	0.650	Conditions not imposed, but checked here. η'_{3r} assumed zero.
Set 2	0.284	0.877	-.055	0.695	

One notes from the last table that, in both instances, the antisymmetry conditions pertaining to vortices 1 and 2 (Eqs. (22a-b) and (23a-b)) are satisfied for all practical purposes, as $r_3 - r_6$ are nearly unity. However, the ratios r_7, r_8, r_9, and the velocity component $(\eta'_{2r})_e$, dealing with vortices 2 and 3, show that Eqs. (22c-d) and (23c-d) are not met. The worst violations are associated with the real components which are expected to have little influence on the lift component. Much improved values for $r_7 - r_9$ and $(\eta'_{2r})_e$ could have been attained if the relation (Eq. 19a)

$$\eta'_3 = q_3$$

had been imposed in lieu of assuming the constant velocity

$$\eta'_3 = \eta'_{3r} + i\eta'_{3i} = 0 + i(\eta'_{3i})_b$$

The variations in the lift coefficient c_ℓ during a period are presented for both sets in Fig. 17, and the corresponding trajectories are shown in Fig. 18. Set 2, which represents the case with the further aft feeding points, exhibits smaller lift than Set 1. The maximum c_ℓ is about 0.26, and is substantially different from the experimentally-determined c_ℓ -amplitude of ~ 0.60. (This value of c_ℓ is chosen from

Figure 7 because it is more representative of the c_ℓ -values in the absence of surface effects and for the low Re-range considered). Set 1 gives a maximum c_ℓ of 0.56 which is in reasonable agreement with the present as well as Keefe's experiments (Ref. 16)*. Both sets of calculations yield vortex trajectories which are in qualitative agreement with observation for Re $\cong$ 6,000 shown in Fig.9. Comparison of the trajectories in Fig. 18 with those of Fig. 9, shows that Set 2 gives slightly better results for the downstream movement (i.e., in the direction of the iz-axis) than Set 1; it also exhibits a trajectory closer to the iz-axis, as it should according to the observations.

Set 1 is considered to be the better of the two overall, for it gives closer agreement in c_ℓ, and because its feeding point appears to be nearer to the point where the shear layer was observed to separate from the cylinder.

The calculations based on the Model II approximation show sufficient promise to warrant further exploration of this technique. One refinement may be offered for future studies; the introduction of the equation describing the movement of the third vortex

$$\eta_3' = q_3$$

to replace the initial assumption of η_3' should result in significant improvement in the trajectories as well as in reducing the "kinks" in the c_ℓ -curves. However, an important question dealing with the nonuniqueness of the solution remains to be resolved. It is related to the question of how well one may be able to predict analytically or "measure experimentally" the locations of the feeding points which were seen to be so important in establishing the c_ℓ -levels.

III.5 EXTENSION TO OSCILLATING CYLINDERS

The stationary cylinder was studied first to develop and to test, with least complications, simple potential flow models capable of predicting loads due the antisymmetric vortex shedding behind such bodies. The experience and the results gained from this phase, along with the

* Note that in Ref. 16, Keefe presents his results in terms of rms values for c_ℓ .

experimental observations described in the earlier sections, should be helpful in extending the promising analytical models to the case of the oscillating cylinder. The latter phase of the study has not progressed to the point where fully-developed methods can be offered, and only a possible approach is presented and discussed below.

It has been observed experimentally (cf. Ref. 6) that when the cylinder performs a lateral sinusoidal oscillation, $y = Y \sin(\omega t + \phi_p)$ the vortex shedding "locks in" with the motion frequency $f = 2\pi\omega$ rather than with the (zero-amplitude) Strouhal frequency f_s, provided the reduced frequency of motion $\frac{fD}{V}$ is sufficiently close (say approximately within ± 5 percent) to the Strouhal number. Otherwise, the lift signals show components in both frequencies f and f_s. It will be assumed here that the former condition is met and that the single frequency characteristics of the motion is known.

Discussed here is the situation when the ratio of amplitude to diameter is quite small. To first order in amplitude, the relative wind velocity V_r is of magnitude V_0 throughout a cycle, i.e.,

$$V_r = \sqrt{V_0^2 + (\omega Y \cos(\omega t + \phi_p))^2} \simeq V_0$$

but is oriented at an angle

$$\alpha = \tan^{-1}\left(\frac{\omega Y \cos(\omega t + \phi_p)}{V_0}\right) \simeq \sin^{-1}\left(\frac{\omega Y \cos(\omega t + \phi_p)}{V_0}\right)$$

to the free-stream velocity V_0. To establish the phasing between motion and lateral (lift) force, consider that time during a cycle which would give on a quasi-steady basis the pattern behind the stationary cylinder at the starting time t_b. To this time is associated the orientation angle, α_b,

$$\alpha_b \simeq \sin^{-1}\left(\frac{\omega Y \cos(\omega t_b + \phi_p)}{V_0}\right) \simeq \frac{\omega Y \cos(\omega t_b + \phi_p)}{V_0}$$

which cannot be determined at the start without specifying ϕ_p ; the phase angle ϕ_p will have to emerge from the solution. However, one possible way of starting the solution is to treat ϕ_p as an additional initial parameter and to determine it by an iterative manner (in much the same manner as the other parameters in the stationary case) which will have to satisfy extended antisymmetry conditions (corresponding to Eqs. (21)-(23) of the stationary case).

Part (a) of Sketch I refers to the starting time t_b . From the stationary cylinder solution, initial conditions on vortices Γ_i , etc. may be imposed, utilizing the instantaneous coordinate system with the imaginary axis along the V_r -direction. For a short time Δt , the cylinder is assumed stationary, and the vortex growths and movements are determined. At the end of this short interval, it is assumed that the cylinder takes its new position $y = Y \sin[\omega(t_b + \Delta t) + \phi_p]$, with the relative wind being in the direction

$$\alpha = \omega Y \cos[\omega(t_b + \Delta t) + \phi_p]$$

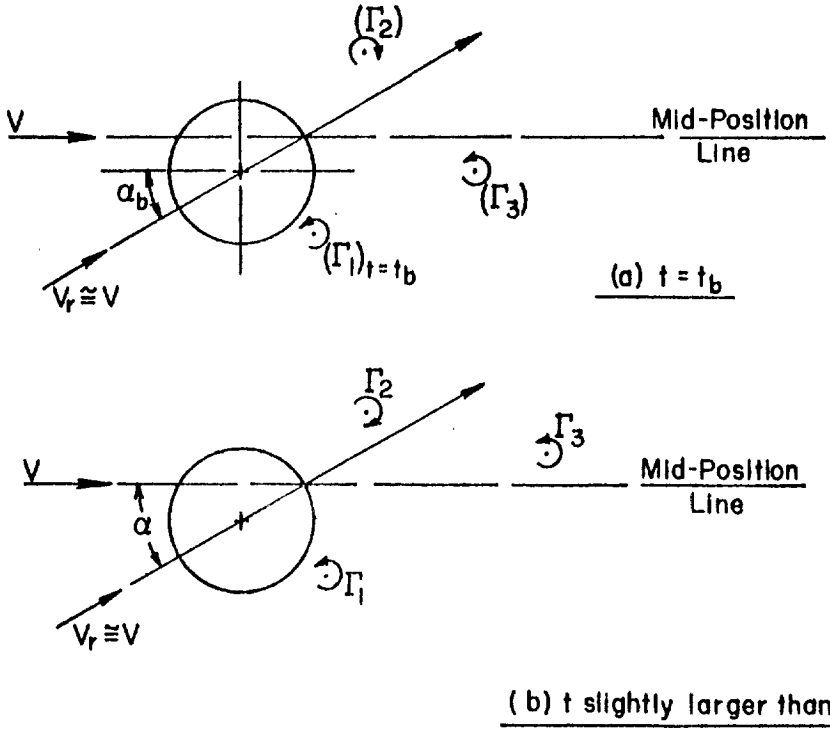

Sketch I. Initial patterns of vortices according to the quasi-steady approach for low amplitude oscillatory motion

For the next interval of time Δt, the solution proceeds in a similar manner, utilizing as initial conditions the results from the previous time interval. At the end of the half period, $t_0 \leq t \leq t_0 + \frac{t_p}{2}$, the conditions must once again become completely antisymmetric; if not ϕ_p (and possibly other initial conditions which were taken from the stationary cylinder solution) will have to be revised.

Whether such a quasi-steady approach yields reasonable estimates of the oscillating loads remains to be determined. There are some modifications that may be introduced. One involves the satisfaction of the boundary condition at the cylinder surface in its mid-position, rather than on the same surface in its instantaneous position. This approximate way of satisfying boundary conditions is frequently introduced in linearized solutions of unsteady flow problems. With the introduction of the latter approximation, it may be possible to abandon the quasi-steady approach, and to formulate a "linearized version", with linearization being with respect to amplitude about the stationary case. To what levels of amplitude these results will be adequate practically is another question which remains to be resolved.

SECTION IV

DISCUSSION OF RESULTS

IV.1 SUMMARY

The effect of model motion on the hydrodynamic forces acting on a circular cylinder can be summarized, in a general way, by two comments:

1. When the amplitude of oscillations is started at a noticeable level, the modification (due to motion) of the force is such as to damp out the motion if the cylinder is left free, unless the reduced frequency of oscillation is close to the Strouhal number.

(2) When operating at reduced frequencies within about ±5 percent of the Strouhal number and at a low but noticeable amplitude level, the hydrodynamic driving force frequency becomes synchronized with the motion frequency. This in turns produces excitation to increase the motion amplitude to the point where structural damping and/or drag (due to lateral motion) just balance the excitation.

For the high mass ratios considered here, and for a natural frequency approximately equal to the Strouhal frequency, free oscillations appear at the natural frequency. Measurements of force and displacement in this situation show negative damping for low amplitudes. The zero hydrodynamic damping boundary is noted only when amplitudes reach the order of the diameter (in the tests reported here, the amplitude of undamped motion was closer to one-half diameter). Thus higher amplitude oscillations are hydrodynamically damped while smaller motions tend to grow. When the natural frequency is not sufficiently close to the Strouhal frequency, only very small self-sustained oscillations are observed. The amplitude of the hydrodynamic force on the cylinder increases with the amplitude of the motion.

The visual studies showed a periodic vortex shedding from alternate sides of the cylinder corresponding to the alternating force. The instantaneous positions of the vortex with respect to the moving cylinder

do not correlate exactly with the positions with respect to a stationary cylinder, even when the changing direction of the relative flow is taken into account. However, the general trend is similar in the oscillating and stationary cases. That is, a vortex first appears a short distance downstream of the side of the cylinder, moves downstream and toward the centerline of the wake, and then, after separating from its feeding sheet, drifts rapidly downstream and slightly outward. Thus, it appears that a quasi-stationary analytical model might reasonably represent the flow about the oscillating cylinder.

Preliminary studies of the effects of neighboring structures, represented by cylinders of various diameters show few unexpected results. When the two cylinders are far apart, their flow fields are independent while, when they are very close together, they produce an oscillating wake with a lower frequency associated with the larger body. However, the transition from the lower frequency to the higher one is not monotonic; the highest frequencies (mixed with other frequencies) occuring at intermediate positions. When one cylinder was directly downstream of the other, the Strouhal oscillations disappeared for some separation distances. This observation may be an important clue in the search for methods of eliminating destructive oscillations of launch vehicles.

Analytical models of the oscillating wake behind a stationary cylinder allow calculations of the vortex motion and corresponding Strouhal forces. For well chosen parameters, the computed results agree quite well with experiment. Extension of this analysis by allowing the stream to change direction relative to the cylinder, in consequence of the cylinder's motion, and thereby representing the oscillating case has been indicated but not completed.

IV.2 CONCLUSIONS

The observations lead to the following characterization of the effect of motion on the Strouhal phenomenon at subcritical Reynolds numbers. When a circular cylinder oscillates at a reduced frequency within ±5 percent of the Strouhal number, the motion is accompanied by an alternate vortex shedding which produces a sinusoidal hydrodynamic force in phase

with the motion over part of each cycle. When the amplitude is small, the work done by this force on the cylinder during the in-phase part of the cycle exceeds that absorbed during the remainder of the period; hence the motion is negatively damped. When the amplitude is greater than about one half the cylinder diameter, the out-of-phase component predominates, and the motion is damped. In the present measurements, the damping is zero when the amplitude is of the order of one diameter (somewhere between .5D and 1D).

The oscillating force on a stationary cylinder can be predicted with fair accuracy by a discrete vortex model. Comparison of vortex paths for stationary and oscillating cylinders indicates some hope for success of a quasi-steady extension of the analysis to the nonstationary case.

Neighboring bodies, represented by additional cylinders completely alter the vortex-shedding phenomenon. It is not valid to neglect the influence of a downstream body on its more upstream neighbor. The mutual interaction may be very strong, and in some tandem arrangements the usual oscillatory wake flow does not appear.

IV.3 FUTURE CONSIDERATIONS

It is obvious that further studies of the launch vehicle problem are needed since no procedure is available for designing, with complete confidence, a satisfactory nonvulnerable structure. Extensions of the present efforts to obtain an understanding of the basic phenomena might be classified under four categories. One area, certainly, would be the completion of studies of the two-dimensional circular cylinder. Analysis of the oscillating model would be included in this category and, perhaps, extension to supercritical Reynolds numbers. A second addition should be the consideration of structural properties. Although it may be easy, in principle at least, to account analytically for structural response, experimental checks with properly scaled aeroelastic models present some difficulties.

One of the least understood and most important aspects of the launch vehicle problem involves the correct application and extension of

two-dimensional information to the real three-dimensional problem. Wind profiles varying over the vehicle in both direction and magnitude should be considered as well as variation in vehicle cross section including the important nose effects.

Other geometrical problems might conveniently be regarded as making up a fourth category for future study. The effects of umbilical towers and other blocking structures deserve further consideration both as necessary parts of the environment of the vehicle and as possible means to alleviate the ground wind problem. Other geometrical fixes, such as strakes, gaps, and tripping devices might also be examined.

In all cases, good results are likely to be achieved when controlled but realistic experiments are combined with detailed examination of the more important factors influencing the ground wind loads.

APPENDIX

The forces on the cylinder may be computed using Blasius' theorem extended to cover unsteady flow or considering the rate of change of the total impulse associated with all vortex pairs in the flow. By introducing in the latter a slight modification necessitated by the flow field approximations, it is shown that these two well-known methods lead to the same force expressions*.

A. METHOD USING BLASIUS' THEOREM

Milne-Thompson (Ref. 32) gives the following expression for the force on the cylinder (translated to the present notation):

$$(L+iD) = -\frac{i\rho}{2}\oint \overline{\left(\frac{dw}{d\zeta}\right)^2}\, d\zeta - i\rho\frac{\partial}{\partial t}\oint w\, d\zeta \qquad (A.1)$$

where L and D are lift and drag forces respectively. The complex potential w and velocity $\frac{dw}{d\zeta}$ are given by Eqs. (7) and (8). The integrations are carried out once around the cylinder surface. The first of these is evaluated using contour integration and the theorem of residues. In the second integral, logarithmic functions appear in the integrand; this necessitates a separate branch cut between each vortex and its image before the contour integrations are carried out. Observing this precaution, the following relations are derived

$$\frac{\partial}{\partial t}\left[\Gamma_\mu \oint \ln\left(\frac{\zeta-\zeta_\mu}{\zeta-\frac{a^2}{\bar\zeta_\mu}}\right) d\zeta\right] = \begin{cases} -2\pi i\left[\dot\Gamma_1\left(\zeta_0-\frac{a^2}{\bar\zeta_1}\right)+\Gamma_1\frac{a^2}{\bar\zeta_1^2}\dot{\bar\zeta}_1\right] & \mu=1 \\ -2\pi i\left[\dot\Gamma_2\left(-\bar\zeta_0-\frac{a^2}{\bar\zeta_2}\right)+\Gamma_2\frac{a^2}{\bar\zeta_2^2}\dot{\bar\zeta}_2\right] & \mu=2 \\ -2\pi i\,\dot\Gamma_\mu\frac{a^2}{\bar\zeta_\mu^2}\dot{\bar\zeta}_\mu & \mu=3,c \end{cases} \qquad (A.2)$$

* In Ref. 23, Ujihara experienced some difficulty in demonstrating the equivalence of these two methods for his model.

Utilizing Eqs. (A.2), the second integral in (A.1) is evaluated. After much algebra, the expression for the force turns out to be

$$(L+iD)_{el.} = \rho\left[V_0\left\{\sum_{s=1}^{3}(-1)^s\Gamma_s\left(1+\frac{a^2}{\bar{\zeta}_s^2}\right)+\Gamma_c\right\}-ia^2\sum_{s=1}^{3}(-1)^s\Gamma_s\frac{\dot{\bar{\zeta}}_s}{\bar{\zeta}_s^2}\right.$$
$$+i\dot{\Gamma}_1\left(\zeta_0-\frac{a^2}{\bar{\zeta}_1}\right)+i\dot{\Gamma}_2\left(\bar{\zeta}_0+\frac{a^2}{\bar{\zeta}_2}\right)+\frac{\Gamma_c}{2\pi}\sum_{s=1}^{3}(-1)^s\Gamma_s\frac{1}{\bar{\zeta}_s}+\sum_{s=1}^{3}\frac{\Gamma_0^2}{2\pi}\frac{1}{\bar{\zeta}_s-\frac{a^2}{\zeta_s}}$$
$$\left.+\frac{1}{2\pi}\sum_{s=1}^{2}\sum_{r=s+1}^{3}(-1)^{s+r}\Gamma_s\Gamma_r\left(\frac{1}{\bar{\zeta}_s-\frac{a^2}{\zeta_r}}+\frac{1}{\bar{\zeta}_r-\frac{a^2}{\zeta_s}}\right)\right] \qquad \text{(A.3)}$$

In the above, the conditions that $|\zeta_c|$ approaches ∞ and $|\dot{\zeta}_c|$ is finite are utilized.

B. METHOD USING THE TOTAL IMPULSE

The total force on the cylinder, according to the impulse method, is given by Eq. (16),

$$(L+iD)_{Im} = \rho\left[-i\sum_{s=1}^{2}(-1)^s\dot{\Gamma}_s\left(\zeta_s-\frac{a^2}{\bar{\zeta}_s}\right)-i\sum_{s=1}^{3}(-1)^s\Gamma_s\left(\dot{\zeta}_s+\frac{a^2}{\bar{\zeta}_s^2}\dot{\bar{\zeta}}_s\right)\right.$$
$$\left.-i\Gamma_c\left(\dot{\zeta}_c+\frac{1}{\bar{\zeta}_c^2}\dot{\bar{\zeta}}_c\right)\right] \qquad \text{(A.4)}$$

Before direct comparison can be made between Eqs. (A.3) and (A.4), certain substitutions must be introduced in (A.4). These involve the relations which impose zero net force on each growing vortex and its feeding sheet (see Eqs. 14):

$$\dot{\zeta}_1+(\zeta_1-\zeta_0)\frac{\dot{\Gamma}_1}{\Gamma_1}=V_0Q_1, \quad \therefore \dot{\Gamma}_1\zeta_1+\Gamma_1\dot{\zeta}_1=\Gamma_1V_0Q_1+\dot{\Gamma}_1\zeta_0$$

$$\dot{\zeta}_2+(\zeta_2+\bar{\zeta}_0)\frac{\dot{\Gamma}_2}{\Gamma_2}=V_0Q_2, \quad \therefore \dot{\Gamma}_2\zeta_2+\Gamma_2\dot{\zeta}_2=\Gamma_2V_0Q_2-\dot{\Gamma}_2\bar{\zeta}_0$$

(A.5a-d)

These expressions, together with those for Q_1, and Q_2 from Eq. (13)*, yield the alternate form for (A.4):

$$(L+iD)_{Sm} = \rho\Big[-\Gamma_1\Big\{V_0\Big(1+\frac{a^2}{\bar{\zeta}_1^2}\Big)+\frac{\Gamma_c}{2\pi}\frac{1}{\bar{\zeta}_1}+\sum_{s=2,3}(-1)^{s+1}\frac{\Gamma_s}{2\pi}\frac{1}{\bar{\zeta}_1-\bar{\zeta}_s}+\sum_{s=1}^{3}(-1)^{s}\frac{\Gamma_s}{2\pi}\frac{1}{\bar{\zeta}_1-\frac{a^2}{\zeta_s}}\Big\}$$

$$+\Gamma_2\Big\{V_0\Big(1+\frac{a^2}{\bar{\zeta}_1^2}\Big)+\frac{\Gamma_c}{2\pi}\frac{1}{\bar{\zeta}_2}+\sum_{s=1,3}(-1)^{s+1}\frac{\Gamma_s}{2\pi}\frac{1}{\bar{\zeta}_2-\bar{\zeta}_s}+\sum_{s=1}^{3}(-1)^{s}\frac{\Gamma_s}{2\pi}\frac{1}{\bar{\zeta}_2-\frac{a^2}{\zeta_s}}\Big\}$$

$$+i\Gamma_1\Big(\zeta_0-\frac{a^2}{\bar{\zeta}_1}\Big)+i\Gamma_2\Big(\bar{\zeta}_0+\frac{a^2}{\zeta_2}\Big)+ia^2\Big(\Gamma_1\frac{\bar{\zeta}_1}{\zeta_1^2}-\Gamma_2\frac{\bar{\zeta}_2}{\zeta_2^2}+\Gamma_3\frac{\bar{\zeta}_3}{\zeta_3^2}\Big)$$

$$+i\Gamma_3\dot{\zeta}_3-i\Gamma_c\dot{\zeta}_c\Big] \qquad \text{(A.6)}$$

When making a comparison between (A.6) and (A.3) (i.e., testing the identity $(L+iD)_{Bl.} = (L+iD)_{Sm}$), one finds that most of the terms in both expressions agree, but that there remain terms in each expression which do not appear reconilable. However, if one introduces in (A.6) the additional relations for the condition that no net force exists on each detached vortex, Eqs. (19a-b),

$$\dot{\zeta}_3 = V_0 Q_3, \quad \dot{\zeta}_c = iV_0 \qquad \text{(A.7)}$$

then the two sides of the "tested identity" show complete agreement.

Since conditions (A.7) have not been imposed in the solutions which yield vortex positions, $(L+iD)_{Bl.}$ and $(L+iD)_{Sm}$ as given by Eq. (A.3) or (A.4) will not agree exactly in numerical calculations. The difference will then be attributed as part of the error in the approximation which omits consideration of Eq. (19a-b). This is not as serious in the calculation of the oscillatory lift, because the major portion of the error turns out to be time-independent.

* The dimensional form of Eq. (9), i.e., in terms of ζ_s' and Γ_s' rather than η_s' and λ_s'.

REFERENCES

1. Foughner, J. T. and Duncan, R. L., "A Full-Scale Ground Wind Load Research Program", Compilation of Papers Presented at the Meeting on Ground Wind Load Problems in Relation to Launch Vehicles, NASA Langley, June, 1966.

2. Rayleigh, Lord, Theory of Sound, Second Edition, Macmillan, London, 1894.

3. Buell, D. A., "Highlights of Ground-Wind Tests at Ames", Compilation of Papers Presented at the Meeting on Ground Wind Load Problems in Relation to Launch Vehicles, NASA Langley, June, 1966.

4. Blackeston, H. S. Jr., "Tip Effects on Fluctuating Air Loads on a Circular Cylinder", AIAA Fifth Annual Structures and Materials Conference, New York, pp. 146-154.

5. Fung, Y. C., "Fluctuating Lift and Drag Acting on a Cylinder in a Flow at Supercritical Reynolds Numbers", J. of the Aerospace Sciences, Vol. 27, No. 11, pp. 801-814, 1960.

6. Meir-Windhorst, A., Flatterschwingungen von Zylindern un gleichmassigen Flussigkeitsstrom, Mitt des Hydraulischen Institute der Technischen Hochschule Munchen, Heft 9, Munich, 1939.

7. Bishop, R. E. D. and Hassan, A. Y., "The Lift and Drag Forces on a Circular Cylinder Oscillating in a Flowing Fluid", Proc. Roy. Soc. A, Vol. 277, pp. 51-75, 1964.

8. Bishop, R. E. D. and Hassan, A. Y., "The Lift and Drag Forces on a Circular Cylinder in a Flowing Fluid", Proc. Roy. Soc. A, Vol. 277, pp. 33-50, 1964.

9. Roshko, A., "Experiments on a Circular Cylinder in a Steady Wind at Transition Reynolds Numbers", Journal of Fluid Mechanics, Vol. 10, p. 345, 1961.

10. Morkovin, M. V., "Flow Around Circular Cylinder – A Kaleidoscope of Challenging Fluid Phenomena", Symposium on Fully Separated Flows, Philadelphia, May, 1964.

11. Scruton, C., On the Wind-Excited Oscillations of Stacks, Towers and Masts, NPL Paper No. 16, Teddington, England, 1963.

12. Whitbread, R.E., "Aerodynamic Excitation of Structures by Wind - A Review of Recent Work at the NPL", Compilation of Papers Presented at the Meeting on Ground Wind Load Problems in Relation to Launch Vehicles, NASA Langley, June, 1966.

13. Reid, W.H., III, "Models for Obtaining Effects of Ground Winds on Space Vehicles Erected on the Launch Pad", Paper Presented at the Conference on the Role of Simulation in Space Technology, Virginia Polytechnic Institute, Blacksburg, Virginia, August 17-21, 1964.

14. Farmer, M.G. and Jones, G.W., Jr., "Summary of Langley Wind Tunnel Studies of Ground-Wind Loads on Launch Vehicles", Compilation of Papers Presented at the Meeting on Ground Wind Load Problems in Relation to Launch Vehicles, NASA Langley, June, 1966.

15. Davenport, A.G., "An Approach to the Wind-Tunnel Modelling of the Response of Structures to the Natural Wind", Compilation of Papers Presented at the Meeting on Ground Wind Load Problems in Relation to Launch Vehicles, NASA Langley, June, 1966.

16. Keefe, R.T., An Investigation of the Fluctuating Forces Acting on a Stationary Circular Cylinder in a Subsonic Stream and of the Associated Sound Field, Univ. of Toronto Rept. UTIA No. 76, September, 1961.

17. Macovsky, M.S., Vortex Induced Vibration Studies, David Taylor Model Basin, Rept. 1190, July, 1958.

18. Humphreys, J.S., "On a Circular Cylinder in a Steady Wind at Transition Reynolds Numbers", Journal of Fluid Mechanics, Vol. 9, p. 603, 1960.

19. Gerrard, J.H., "An Experimental Investigation of the Oscillating Lift and Drag of a Circular Cylinder Shedding Turbulent Vortices", Journal of Fluid Mechanics, Vol. 11, p. 244, 1961.

20. Parkinson, G.V. and Ferguson, N., "Amplitude and Surface Pressure Measurements for a Circular Cylinder in Vortex-Excited Oscillation at Subcritical Reynolds Numbers", Compilation of Papers Presented at the Meeting on Ground Wind Load Problems in Relation to Launch Vehicles, NASA Langley, June, 1966.

21. Cincotta, J.J., Jones, G.W., Jr., and Walker, R.W., "Experimental Investigation of Wind Induced Oscillation Effects on Cylinders in Two-Dimensional Flow at High Reynolds Numbers", Compilation of Papers Presented at the Meeting on Ground Wind Load Problems in Relation to Launch Vehicles, NASA Langley, June, 1966.

22. Bryson, A.E., Jr., "Symmetric Vortex Separation on Circular Cylinders and Cones", Journal of Appl. Mech., pp. 643-648, December, 1959.

23. Ujihara, B.H., An Analytical Study of Separated Flow about a Circular Cylinder, North American Aviation Report SID 65-1730, January, 1966.

24. Wu, P.K.S., An Experimental Study of Wind Induced Launch Vehicle Oscillations, S.M. Thesis, Mass. Inst. of Tech., Dept. of Aero. and Astro., June, 1966.

25. Roshko, A., On the Development of Turbulent Wakes from Vortex Streets, NACA TN 2913, 1953.

26. Geller, E.W., An Electromechanical Method of Visualizing the Boundary Layer, M.S. Thesis, Dept. of Aero. Eng., Miss. State College, August, 1954.

27. Clutter, D.M., Smith, A.M.O., and Brazier, J.C., Techniques of Flow Visualization Using Water as the Working Medium, Douglas Aircraft Co., Report ES29075, April, 1959.

28. Schraub, F.A., Kline, S.J., Henry, J., Rundstadler, P.W., Jr., and Littel, A., Use of Hydrogen Bubbles for Quantitative Determination of Time-Dependent Velocity Fields in Low Speed Water Flow, Thermosciences Div., Dept. of Mech. Eng., Stanford University, Rept. MD-10, February, 1964.

29. Friberg, E.G., Measurement of Vortex Separation, Part I: Two Dimensional Circular and Elliptic Bodies, Aerophysics Lab., M.I.T., Rept. TR 114, August, 1965.

30. Edwards, R.H., "Leading Edge Separation from Delta Wings", Journal of Aero. Sci., Vol. 21, No. 2, p. 134, February, 1954.

31. Hill, J. A. F., "A Nonlinear Theory of the Lift on Slender Bodies of Revolution", NAVORD Report 5338, Proceedings, U. S. Navy Symposium on Aeroballistics, 1954.

32. Milne-Thompson, L. M., Theoretical Hydrodynamics, Fourth Ed., MacMillan, London, 1960.

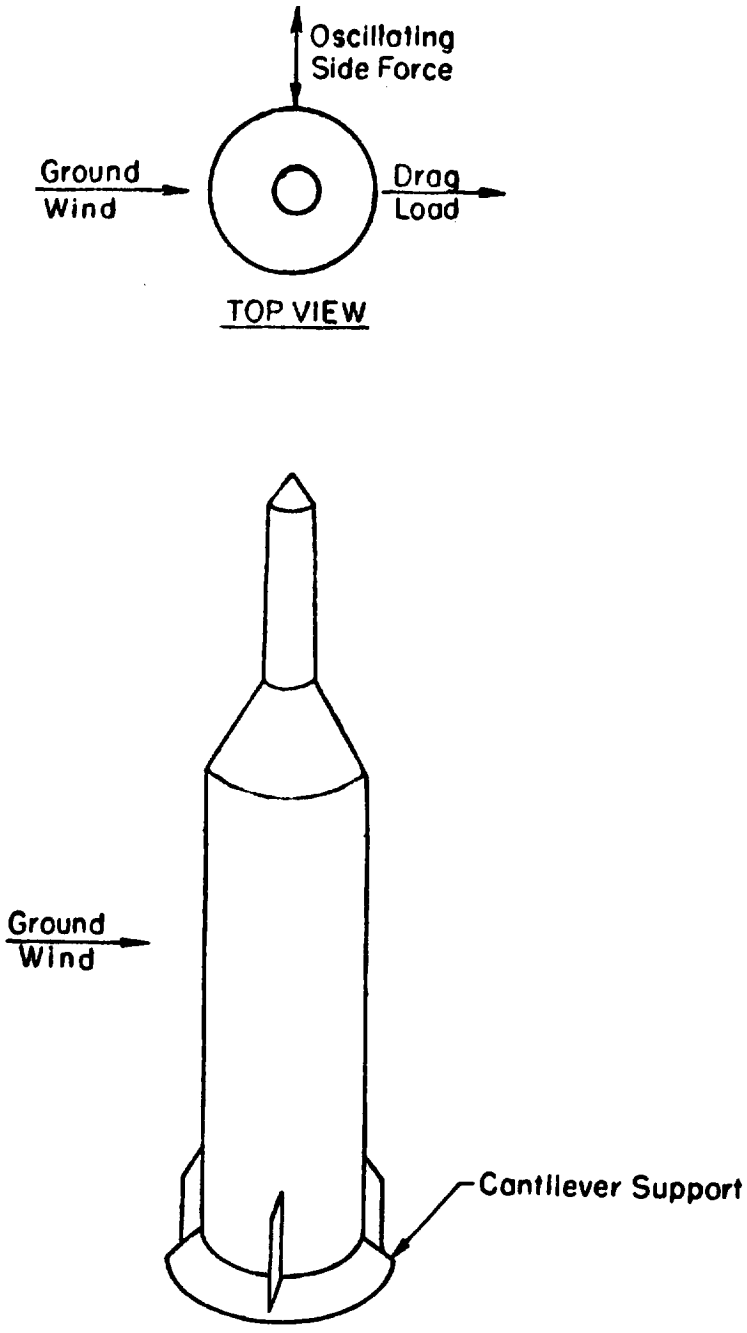

Figure 1. Schematic representation of erected launch vehicle

Figure 2. Water table

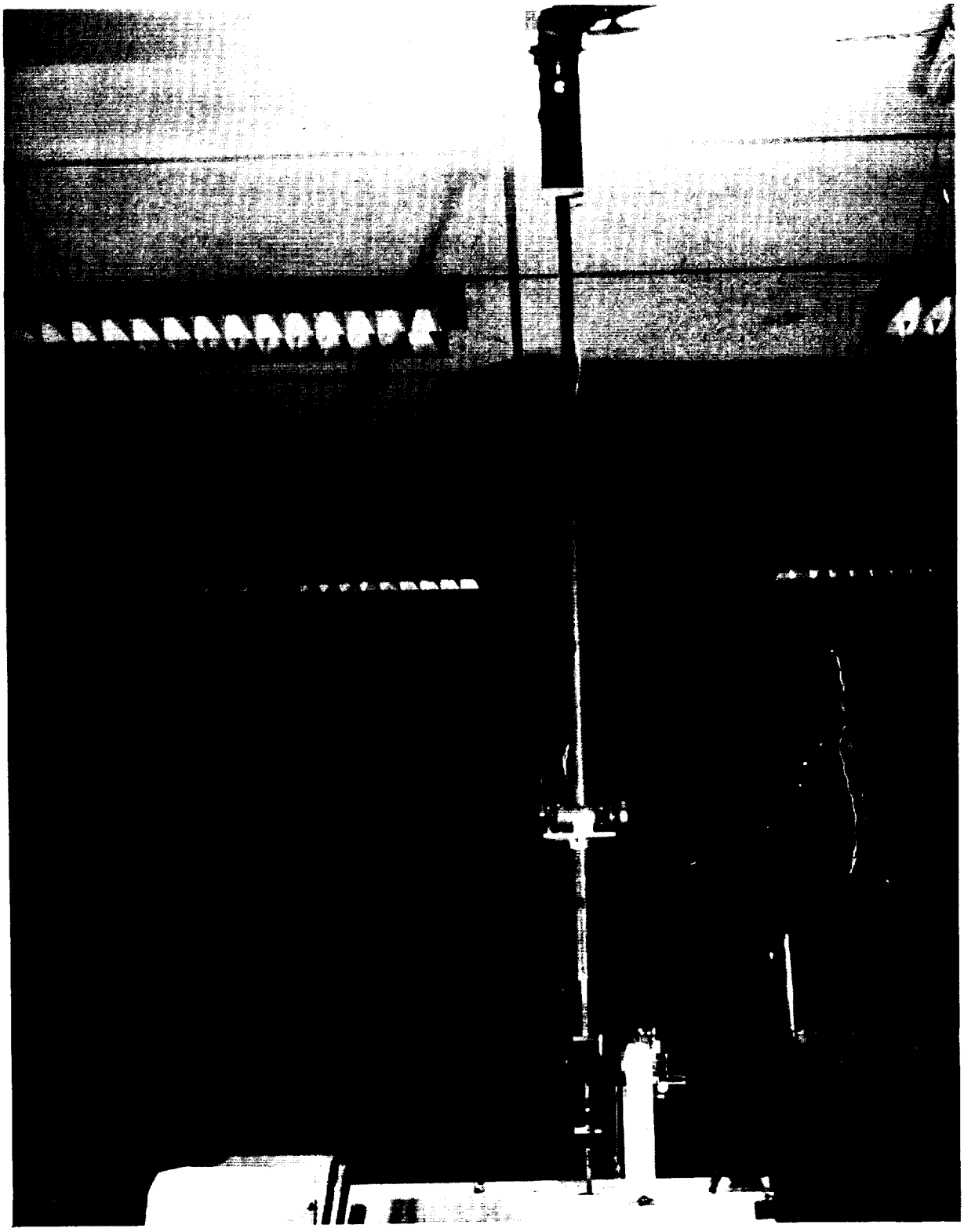

Figure 3. The pendulum

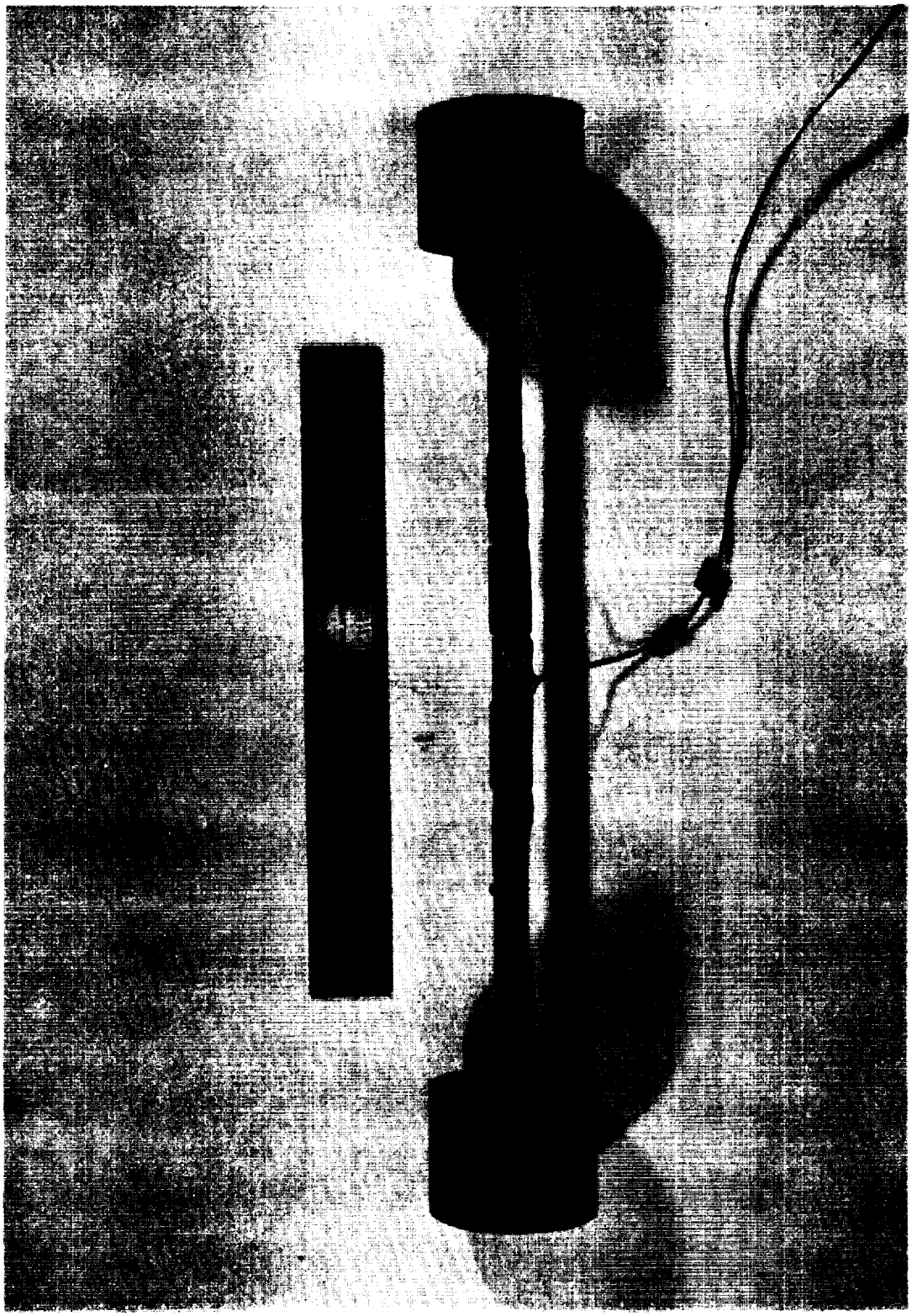

Figure 4. The model

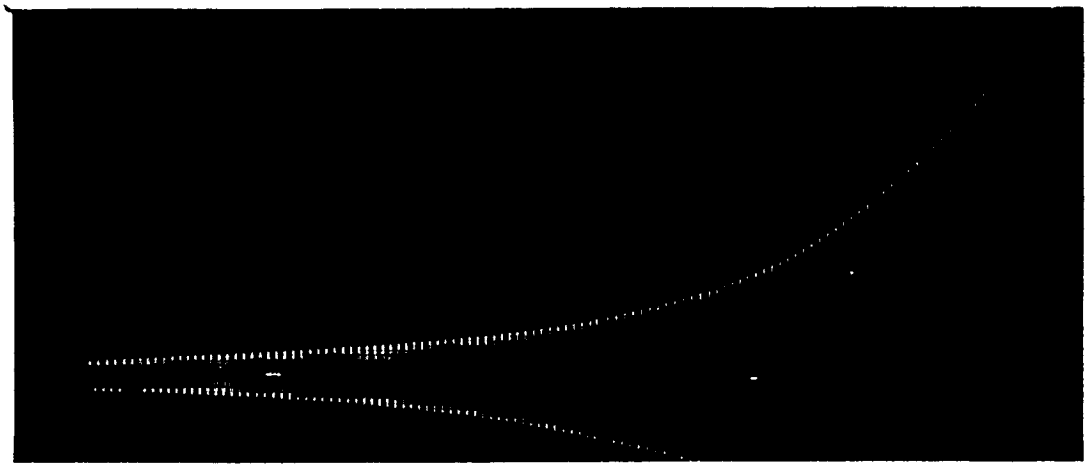

← Time

5(a)

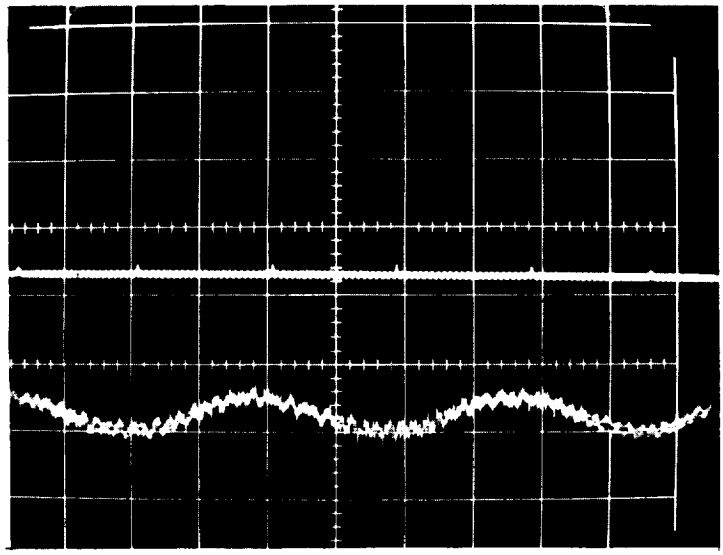

5(b)

Figure 5. Typical force and displacement data

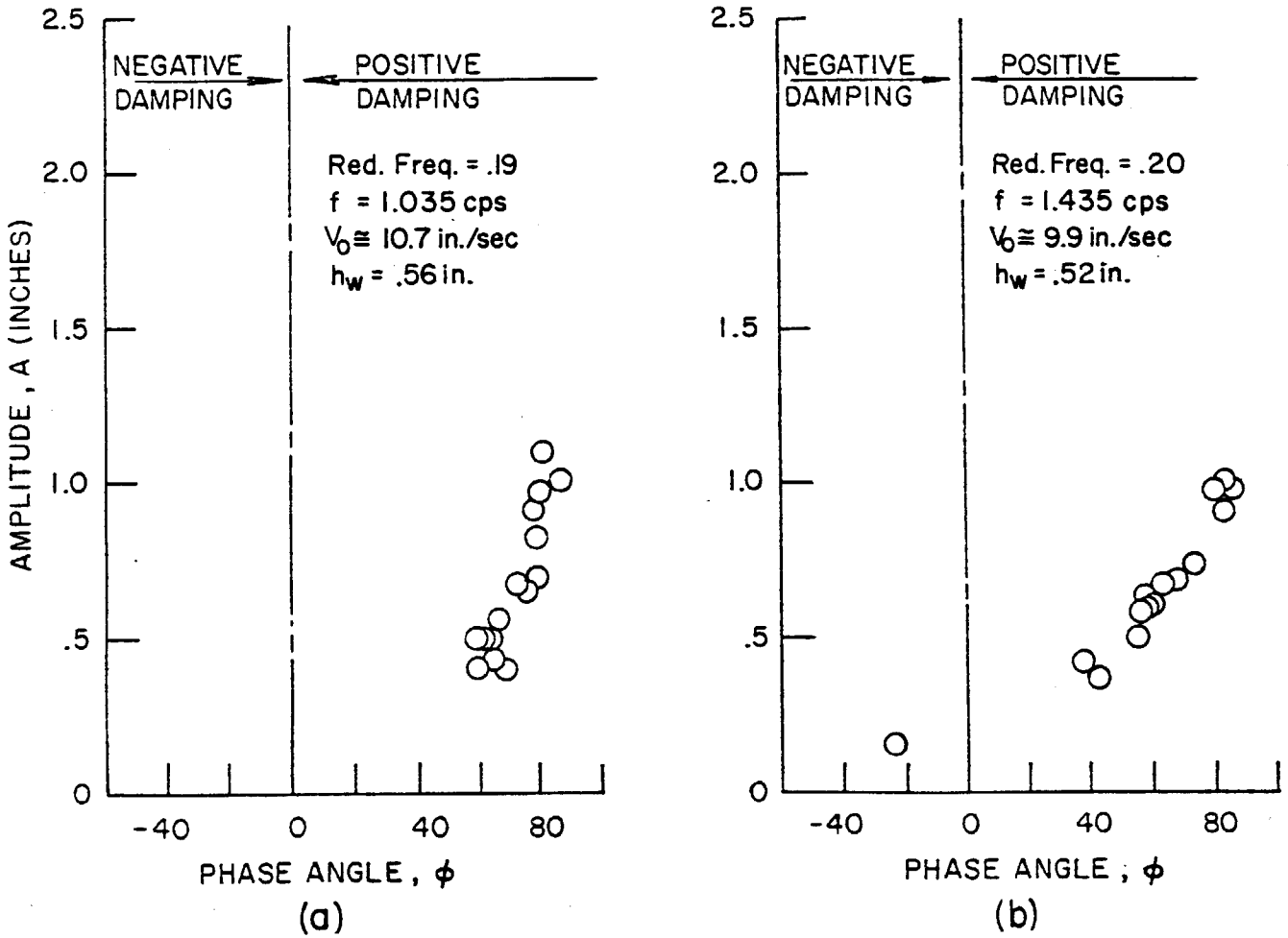

Figure 6. Phase angle vs. amplitude

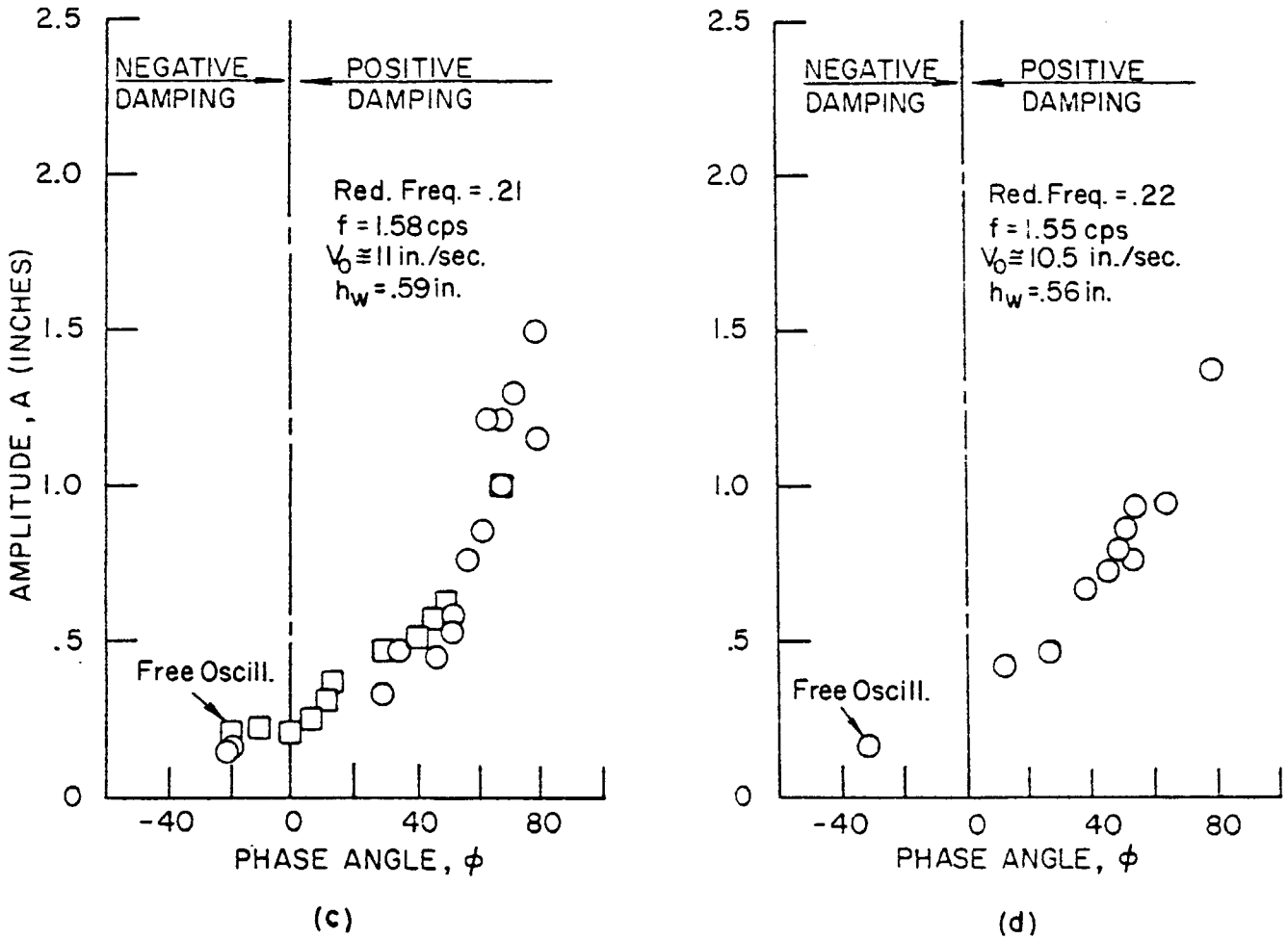

Figure 6 (Continued)

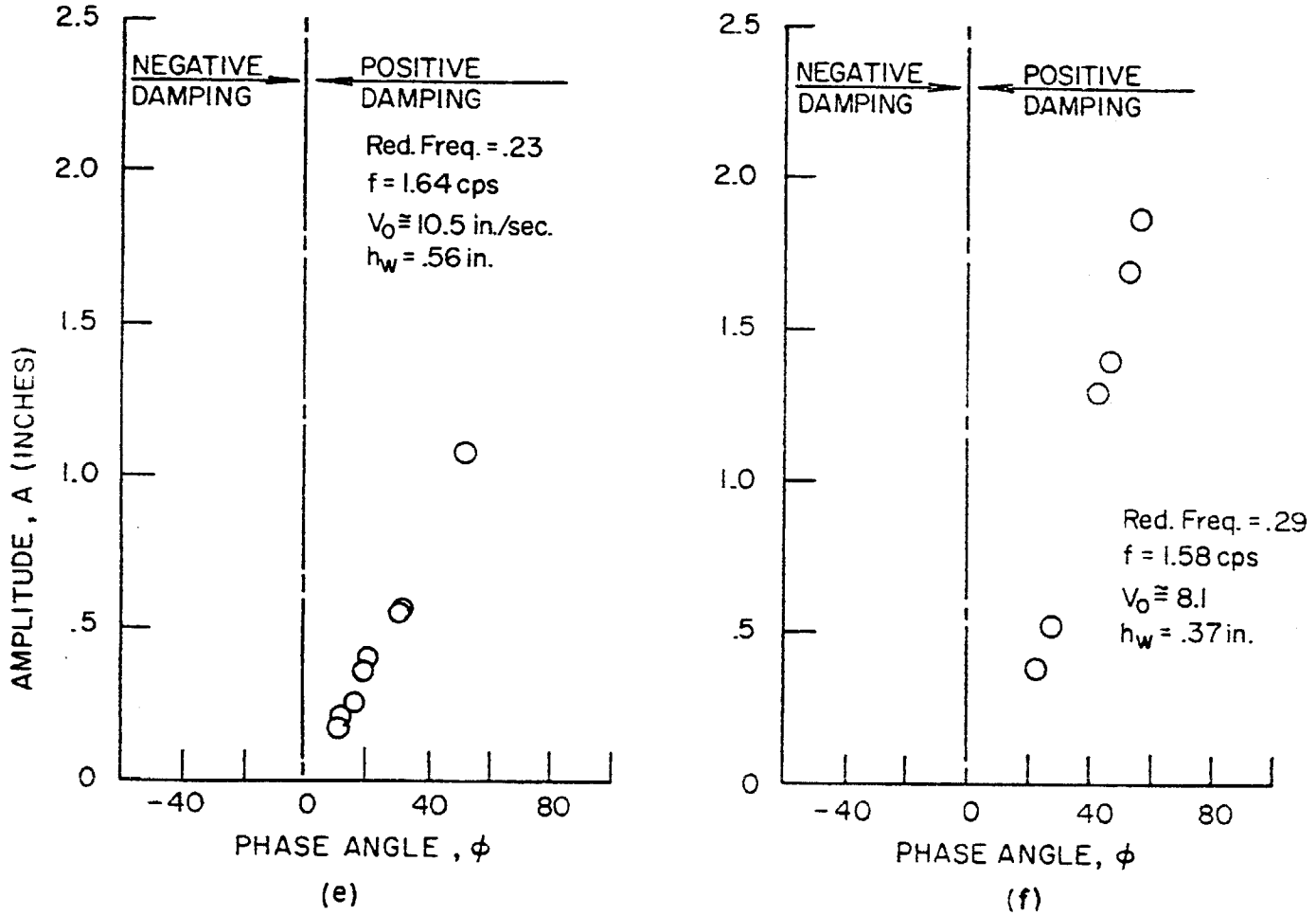

Figure 6 (Concluded)

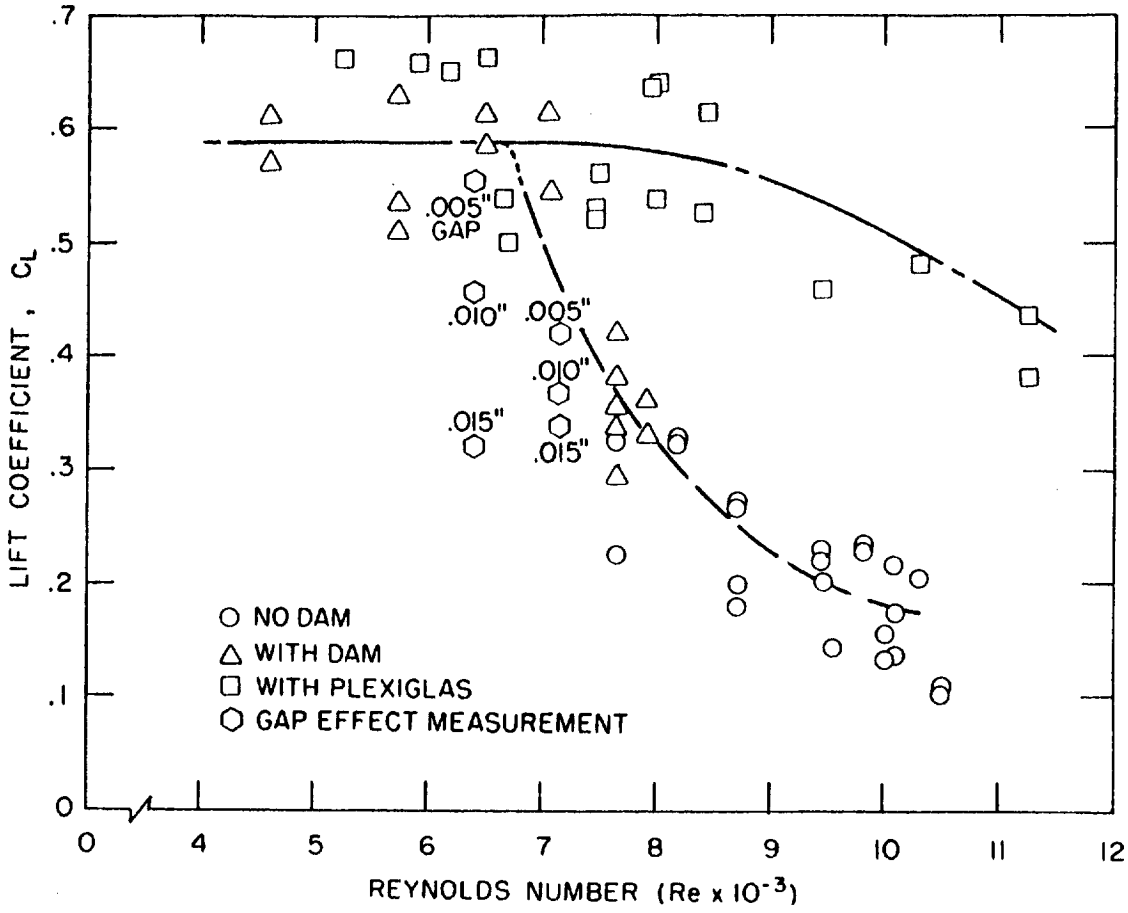

Figure 7. Amplitude of lift coefficient on stationary cylinder

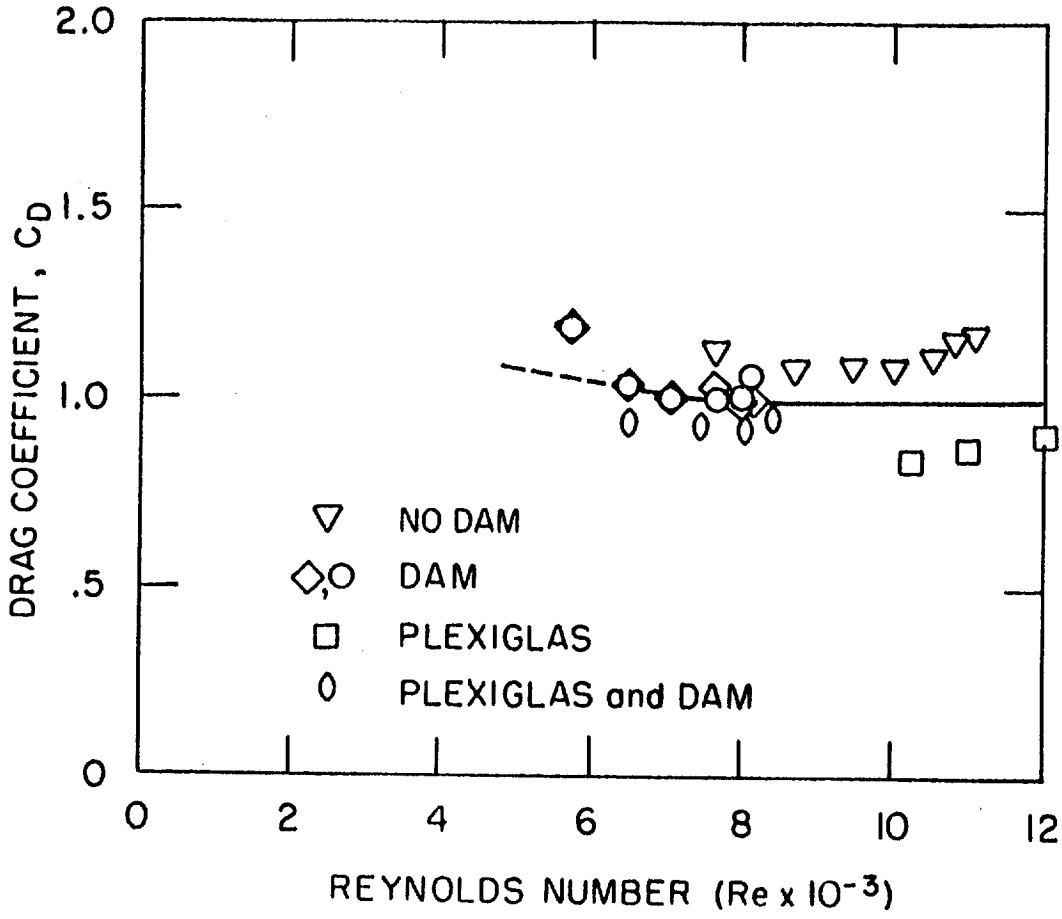

Figure 8. Drag coefficient on stationary cylinder

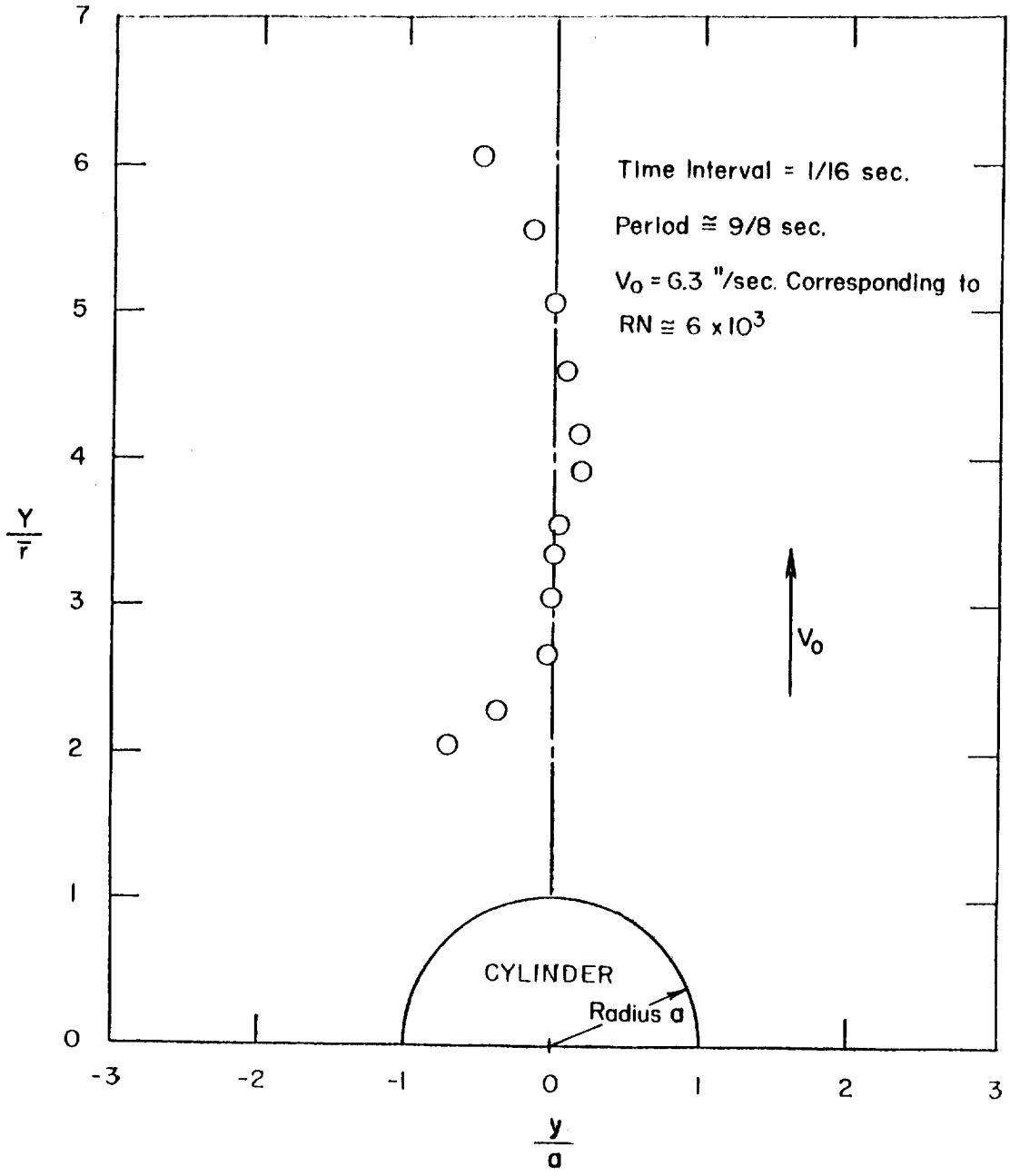

Figure 9. Vortex position behind a stationary cylinder

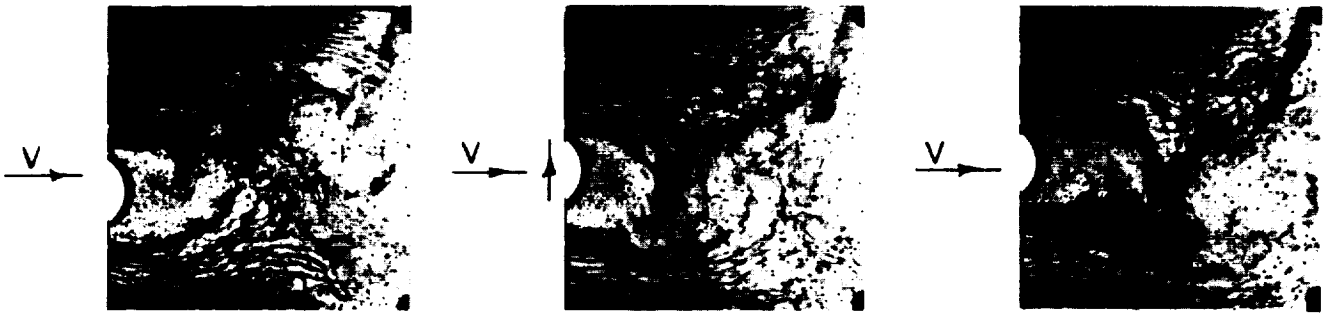

(a) Small Amplitude (A = .25 inch)

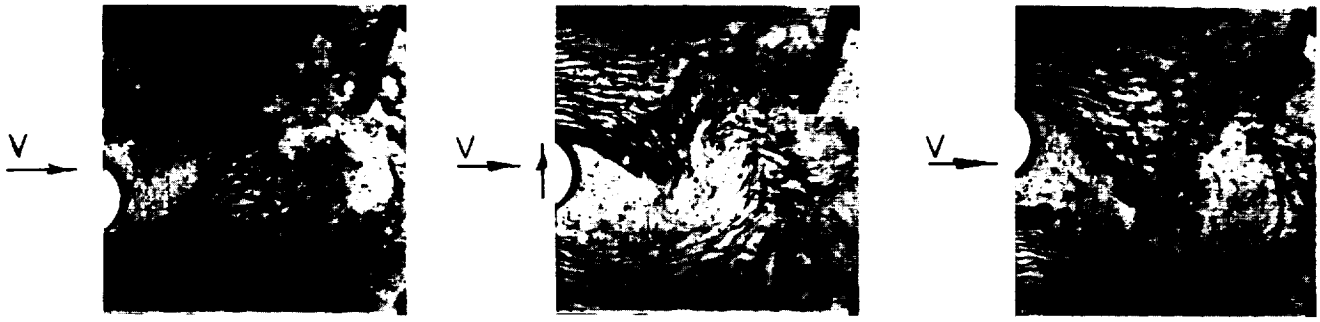

(b) Critical Amplitude (A = 0.70 inch)

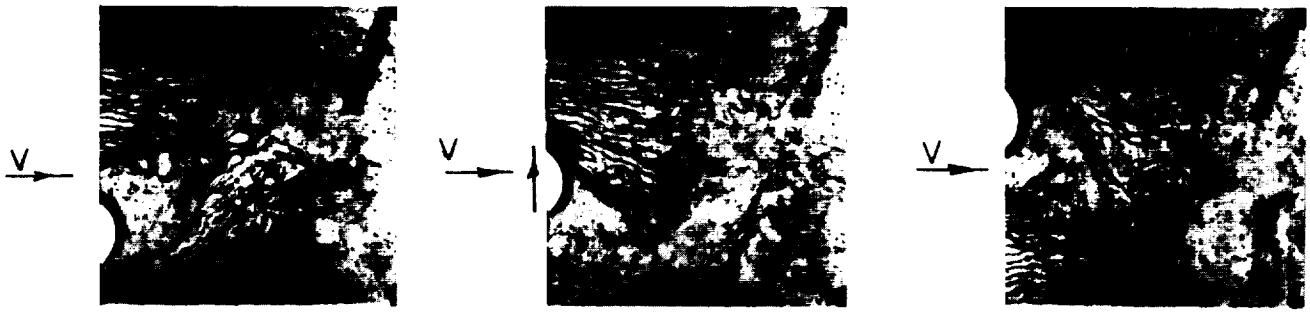

(c) Large Amplitude (A = 1.05 inch)

Figure 10. Flow field behind an oscillating cylinder

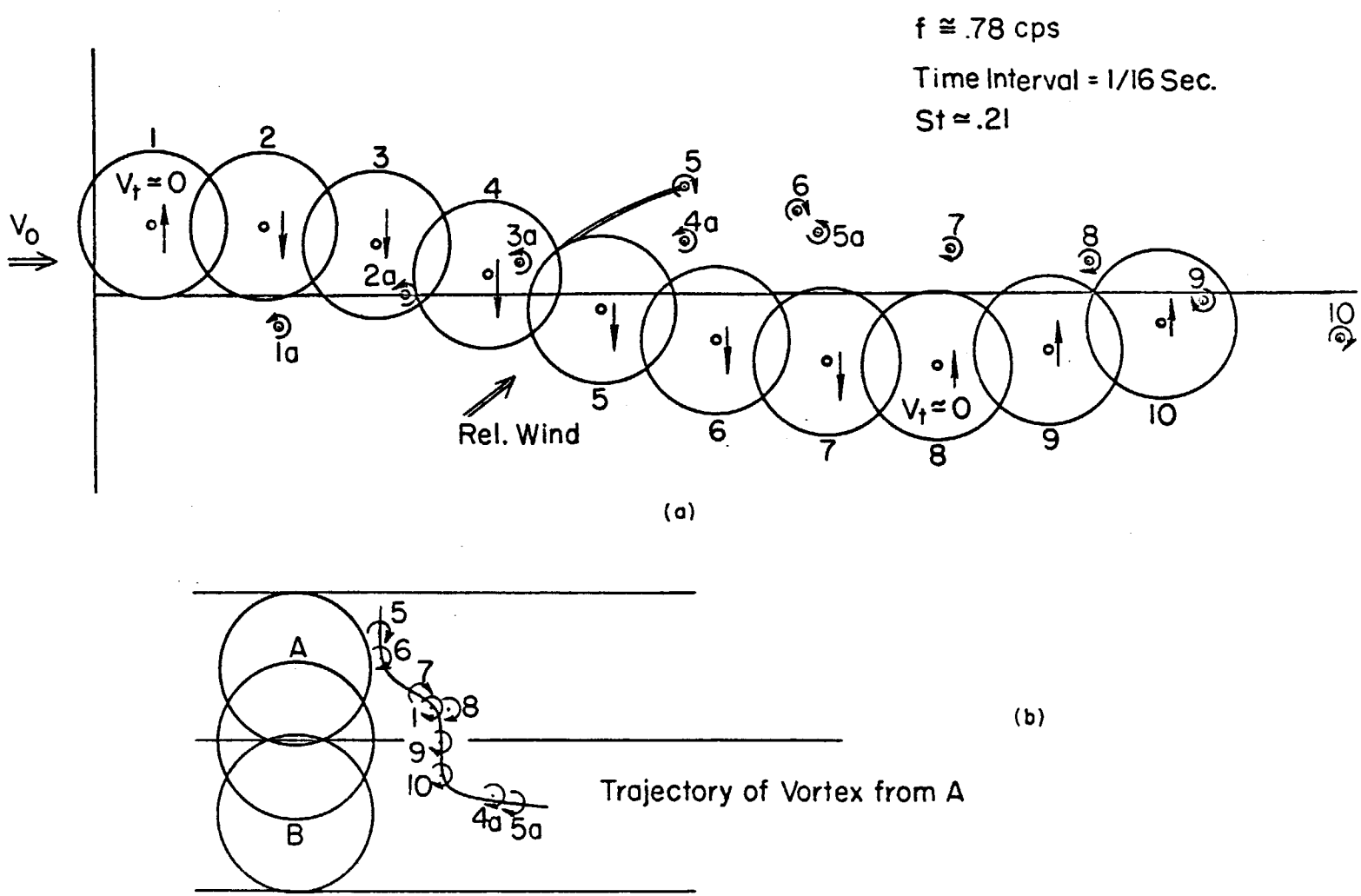

Figure 11. Vortex position behind an oscillating cylinder

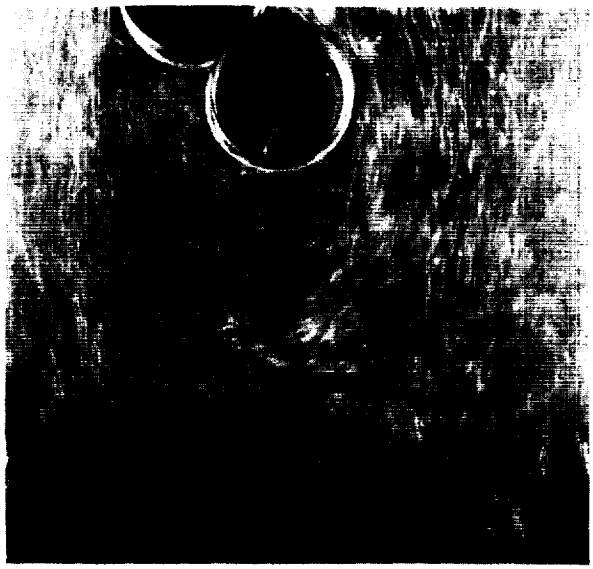

(a) $\ell = 0$

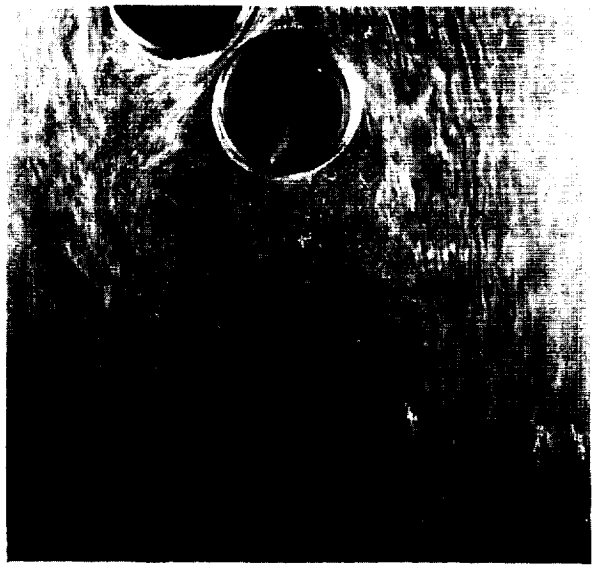

(b) $\ell = .17$

Figure 12. Flow field behind the model with an umbilical tower at $\theta = 45°$ ($D' = 1$)

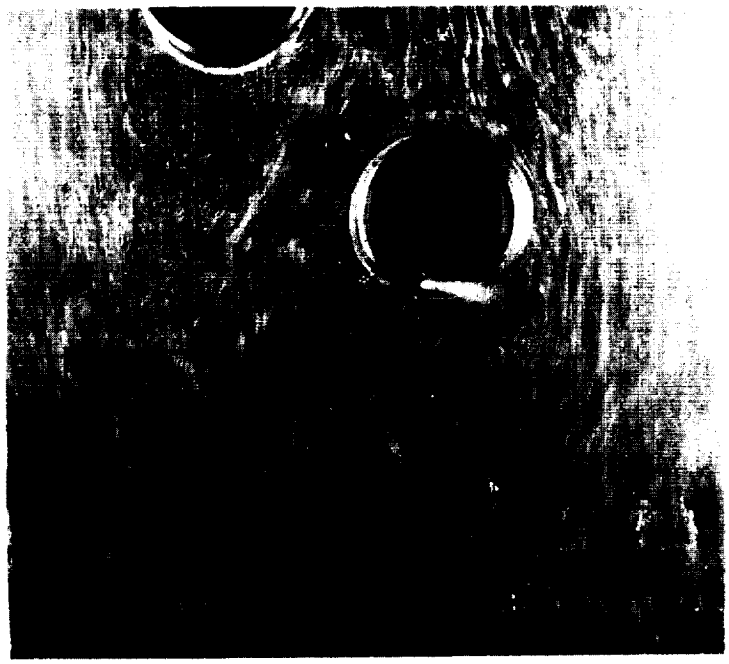

(c) $\ell = 1$

Figure 12. Continued

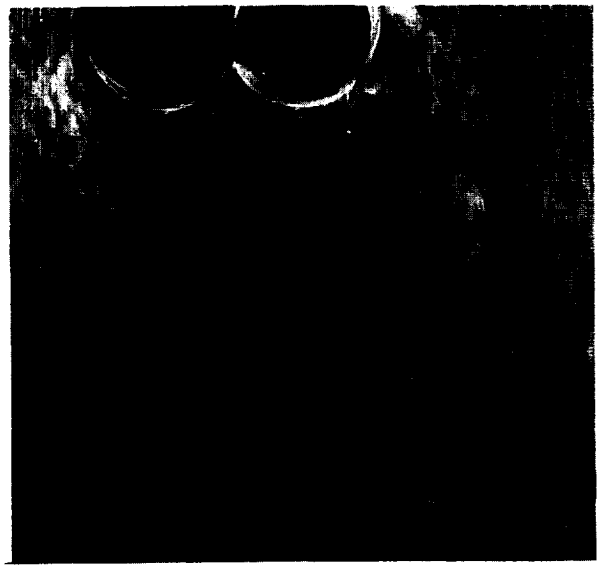

(a) $\ell = 0$

(b) $\ell = 1$

Figure 13. Flow field behind the model with an umbilical tower at $\theta = 90°$ ($D' = 1$)

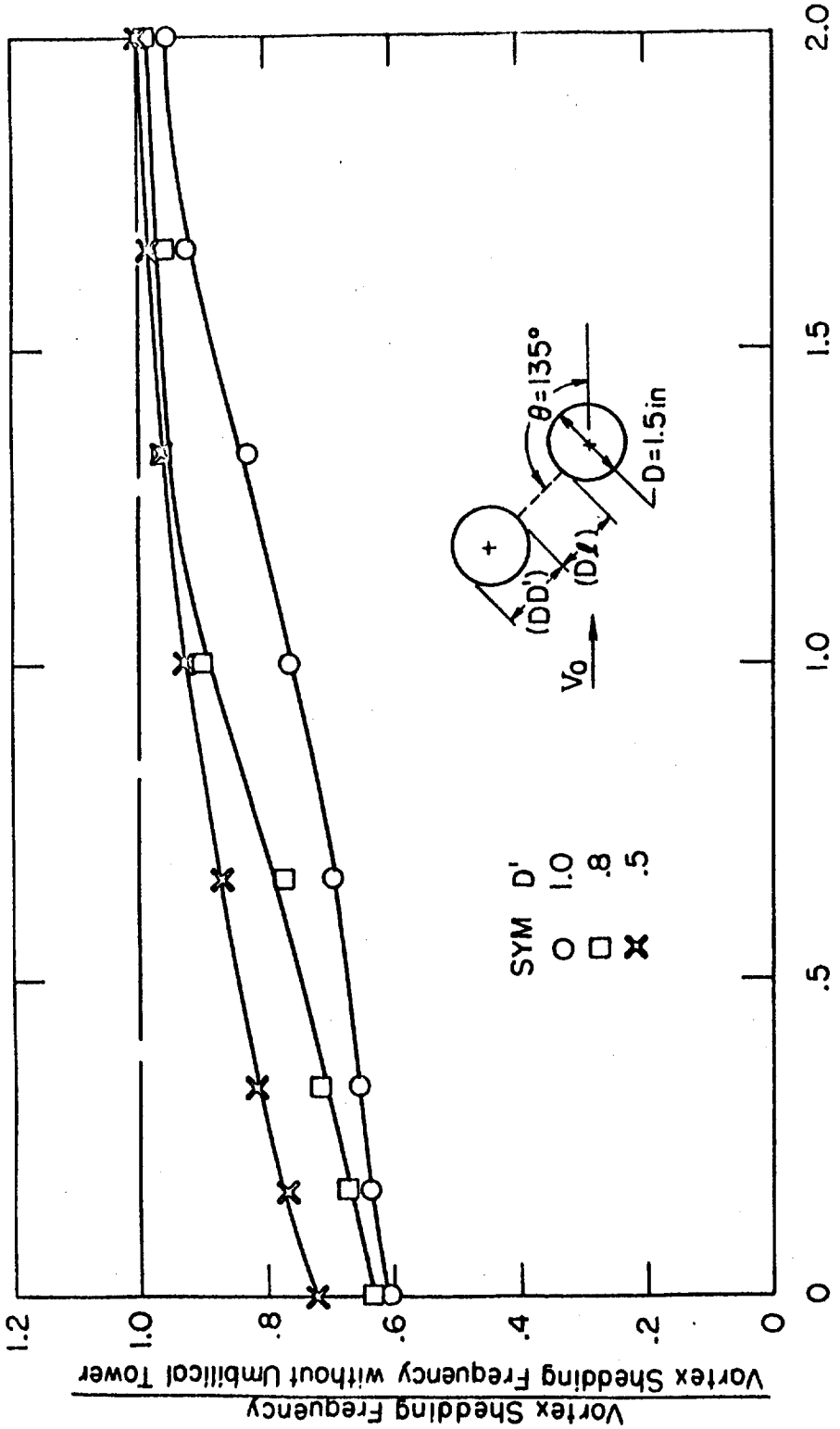

Figure 14. Vortex shedding frequency vs. separation distance for $\theta = 90°$

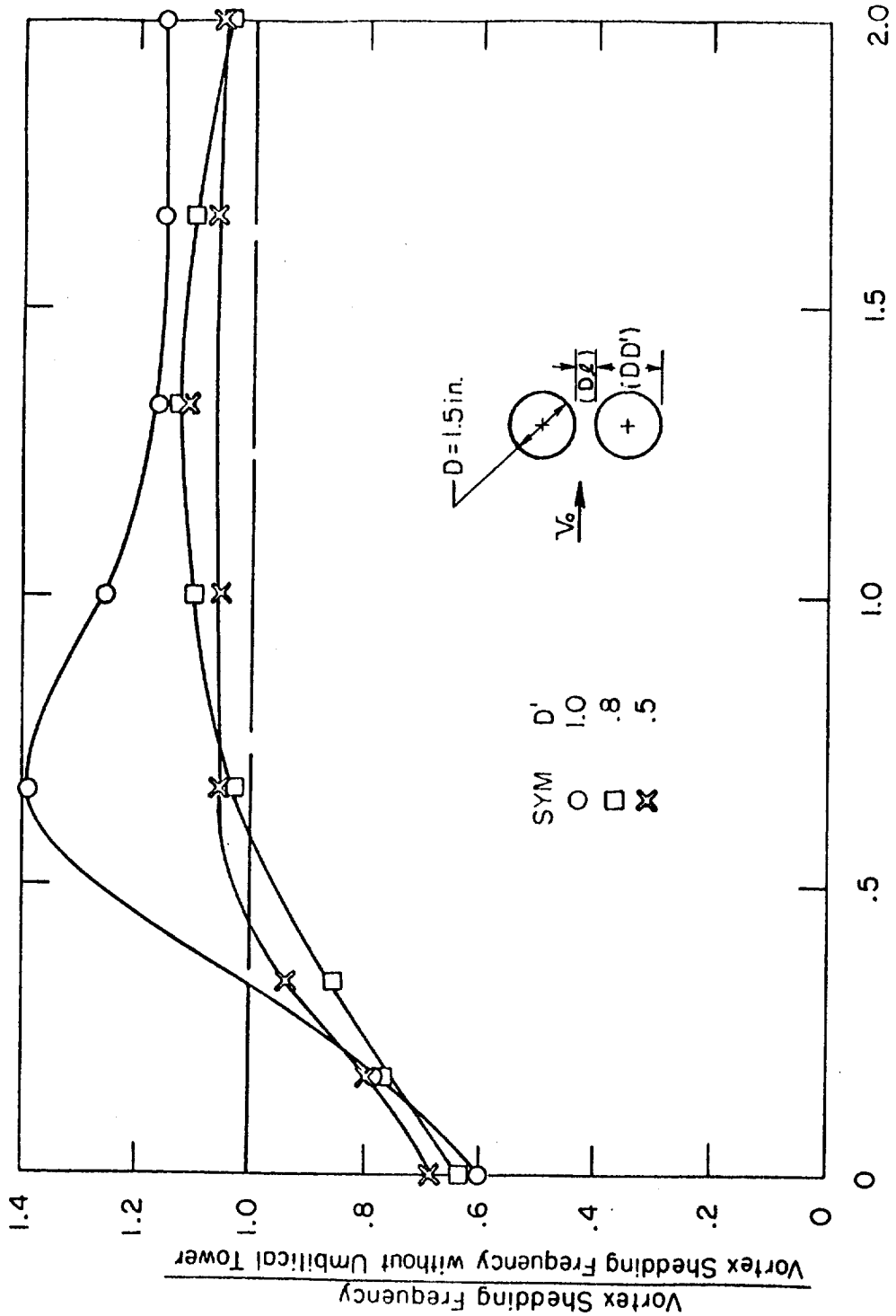

Figure 15. Vortex shedding frequency vs. separation distance for $\theta = 135°$

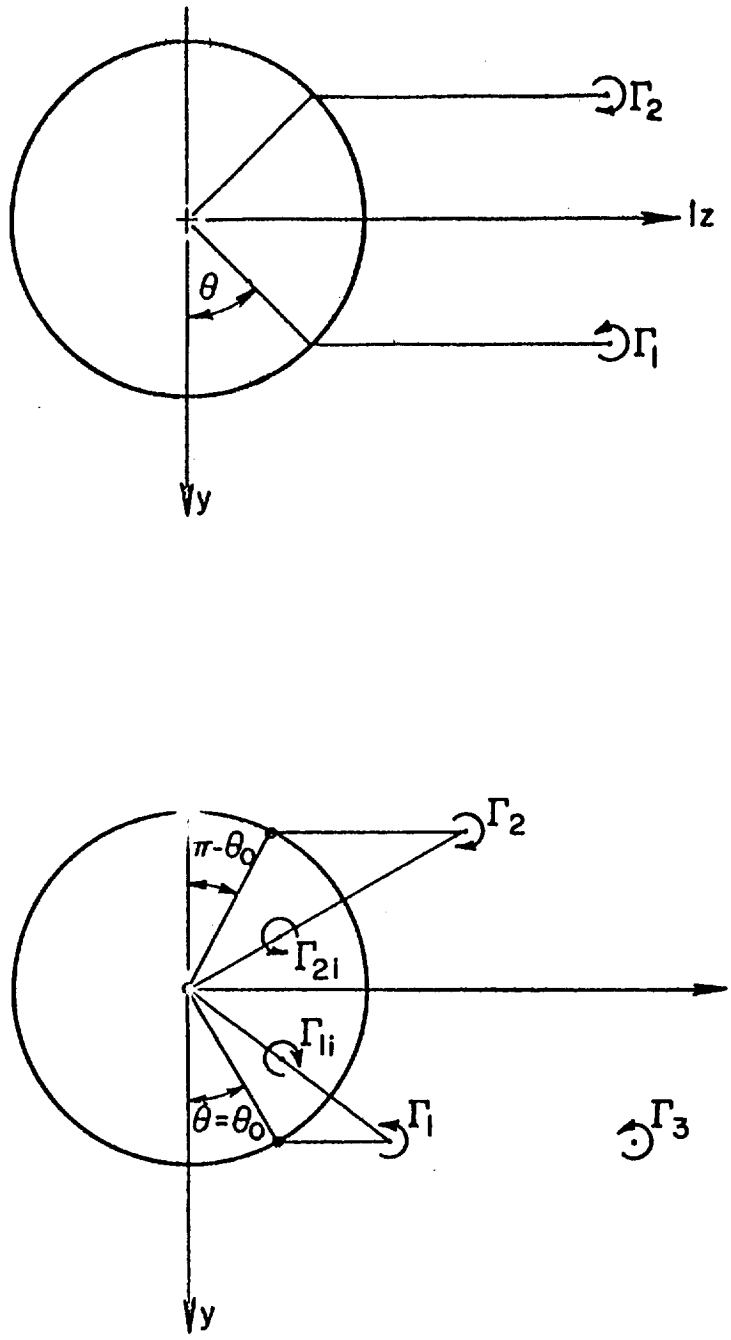

Figure 16. Vortex representation

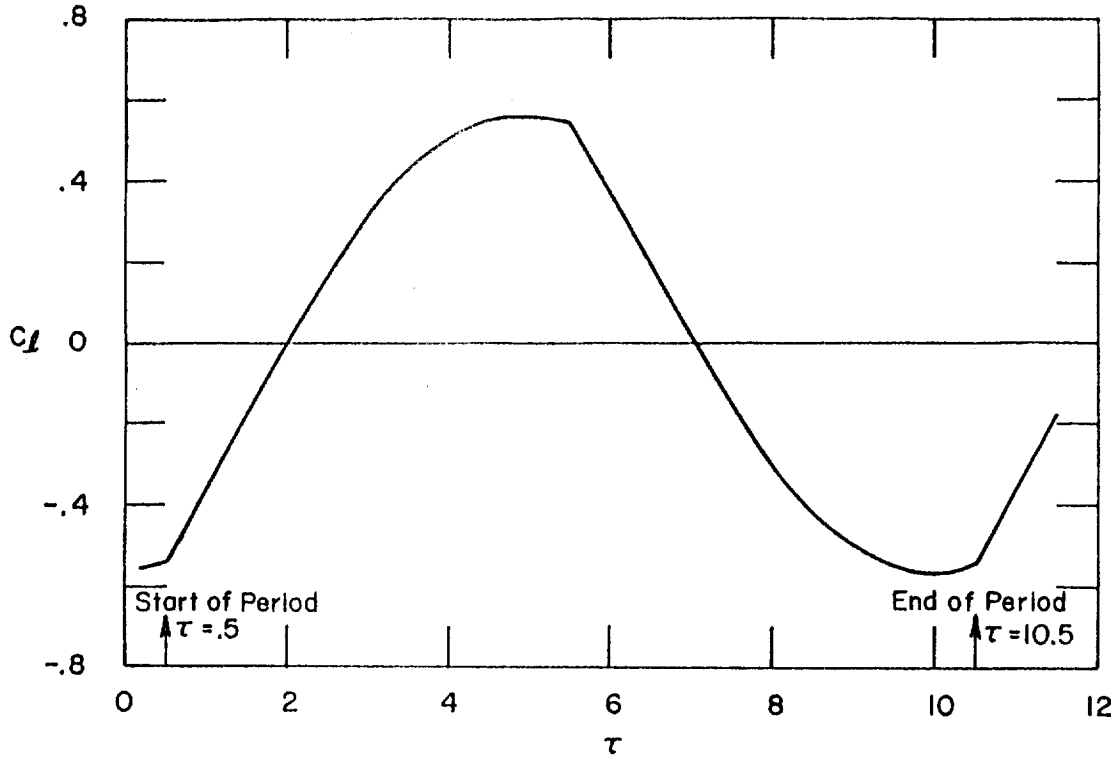

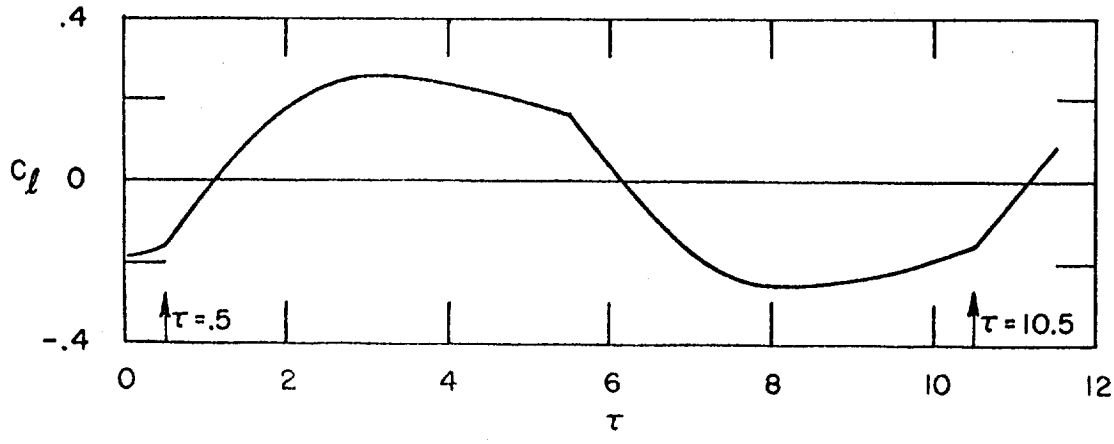

Figure 17. Variation in lift coefficient on stationary cylinder over one cycle

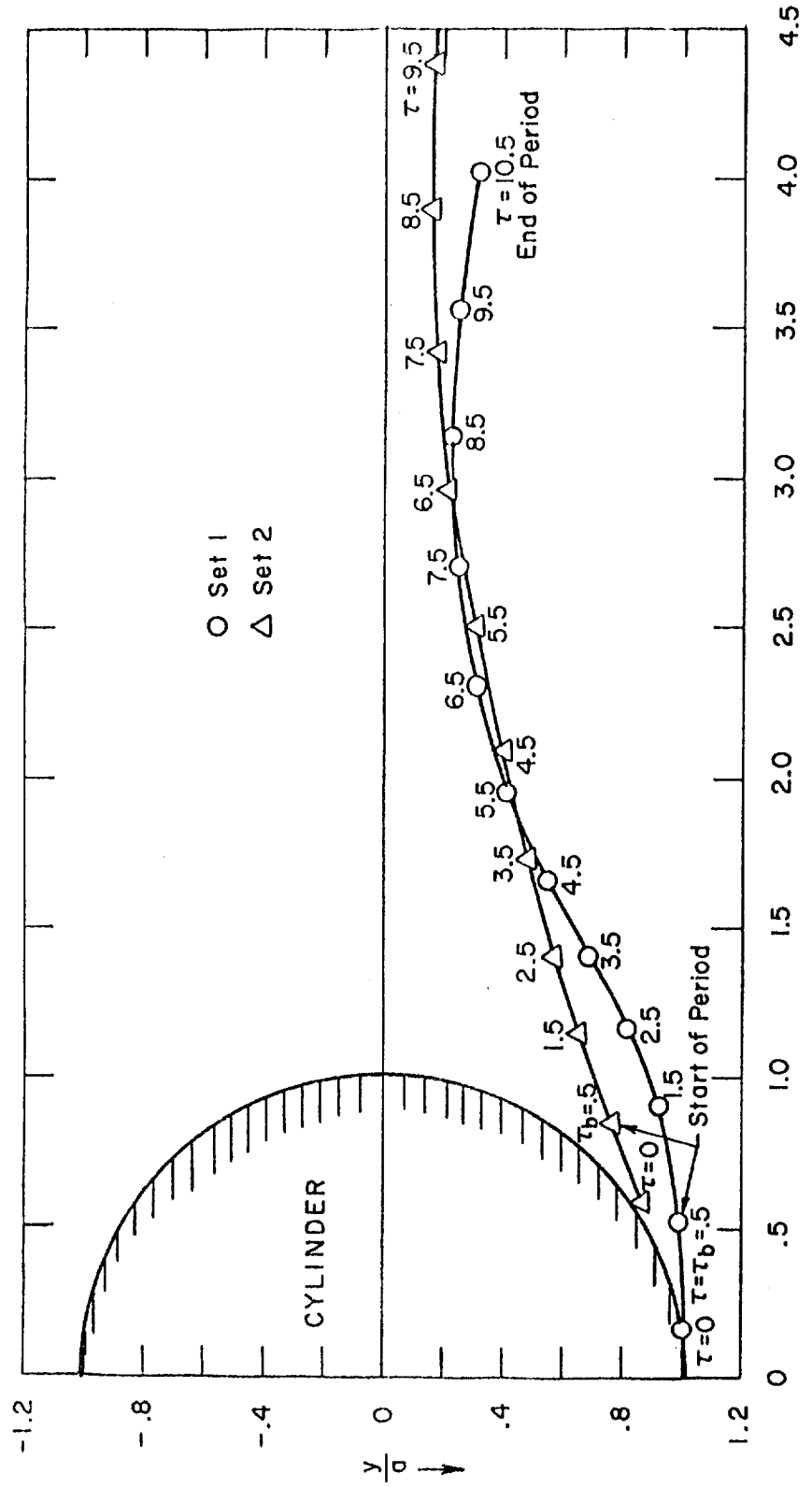

Figure 18. Calculated vortex trajectories behind stationary cylinder